

**Structure -rheology relationship for a homogeneous colloidal gel under shear startup**

**Jun Dong Park**

*Department of Chemical and Biomolecular Engineering, University of Illinois at Urbana-Champaign,  
Urbana, Illinois, 61801*

**Kyung Hyun Ahn**

*School of Chemical and Biological Engineering, Institute of Chemical Process, Seoul National  
University, Seoul, 151-744 Korea*

**Norman J. Wagner\***

*Department of Chemical and Biomolecular Engineering and Center for Neutron Science, University  
of Delaware, Newark, Delaware 19716*

**Abstract**

The structural anisotropy and shear rheology of colloidal gels under startup of shear flow are calculated by Brownian Dynamics simulations modified to include particle surface-mediated attractions, which is a model for thermoreversible colloidal gels. Shear-induced structural changes are analyzed in both real and reciprocal space through computation of the pair distribution function and structure factor. A distinct structural anisotropy is evident as alignment along the compressional and vorticity axes. A spherical harmonics expansion of pair distribution function is calculated to analyze structural anisotropy. In reciprocal space, structural anisotropy is quantified through an alignment factor, which shows overshoot behavior similar to the stresses. Based on the microstructure analysis, the evolution of the structural anisotropy is explained by the anisotropic rupture of the colloidal gel microstructure. This result provides evidence for how shearing creates structural anisotropy. The structural anisotropy during flow startup is quantitatively related to rheological behavior via a stress-SANS rule that is modified to consider the influence of the rupture of the colloidal gel structure. A simple structure kinetic equation accounting for bond creation and rupture provides a unifying view of the results. This new, modified stress-SANS rule *quantitatively* links the shear-induced structural anisotropy to the non-linear rheology.

## I . Introduction

Colloidal particles show rich phase behavior and mechanical properties that depend on the flow conditions, concentration and particulate interactions. Of interest here, at sufficiently high concentrations colloidal particles that interact through attractive forces organize into a space-filling network structure termed a “colloidal gel” [1,2]. The colloidal gels are characterized by solid-like elastic properties, which results from a stress-bearing network structure. In sufficiently strong flows, colloidal gels go through a rupture of the microstructure, which is known as yielding. The yielding behavior reveals itself with a variety of microstructural changes. In recent studies using confocal microscopy [3] and simulations [4,5], this yielding is related to the structural evolution from rigid chains with high coordination number (higher or equal to 4) to soft chains with low coordination number (lower than 4). In another study on dense gels at high volume fraction [6], yielding is considered as two-step process of bond and cage breakage. These structural changes accompany nonlinear rheological behaviors, such as stress overshoot [7], non-sinusoidal stress response [8], and nonlinear creep compliance [9].

The structural anisotropy in colloidal gels induced by flow has been studied extensively through scattering methods including flow-SANS [10] and light scattering [11]. In another work [12], the structural anisotropy was probed across a broad range of length scales utilizing small angle light scattering (SALS), small angle x-ray scattering (SAXS), and ultra-small angle x-ray scattering (USAXS). These results revealed structural anisotropy along the vorticity axis, which is characterized by butterfly pattern in the velocity-vorticity plane. Recently, the development of a new sample environment for SANS under flow enabled determining the structural anisotropy on a shorter length scale corresponding to local microstructure [8,13]. In these works, microstructural changes on the particle length scale were measured in both the velocity-vorticity plane and the velocity-gradient plane. In addition to the butterfly pattern in the velocity-vorticity plane, colloidal gels under steady and dynamic shear flow exhibit structural anisotropy along the compressional axis, which is represented by enhanced scattering pattern along the extensional axis. Such structural anisotropy under flow is also evident in direct visualization using microscopy [14-16] and numerical simulations [4], which make it possible to study structural anisotropy in real space. By correlating structural anisotropy dynamics of aggregates, these studies enhance our understanding of how gels flow.

It has been shown that the microstructural changes, such as the size of aggregates, network bond rupture, or cage breakage, have deterministic effects on the rheological behavior [4-6]. In addition to these size-related microstructural changes, structural anisotropy is important for determining

rheological behavior as directly shown by previous research that studied this specific relationship through theory [17] and microscopy [18,19]. The relationship between structural anisotropy and rheology for colloidal gels has been established for steady shear flow in terms of an inverse Bingham number [13] and quantified in terms of stress-SANS rule [8]. Recent investigations examine transient flows. The qualitative relationship among flow-induced structural anisotropy, yielding, and stress overshoot was investigated in the velocity-vorticity plane [11]. For a colloidal gel with fractal structure, a qualitative correlation was observed between structural anisotropy and rheology [20]. In this study using small-angle light scattering, both structural anisotropy in the plane of flow and shear stress response showed overshoot behavior and their maxima coincided. In recent work [8], shear induced structural anisotropy was studied under large amplitude oscillatory shear (LAOS). This work showed how the structural anisotropy is correlated to the non-linear rheological behavior and developed the first “structure Lissajous-Bowditch” diagrams to illustrate this for LAOS flows. Such a direct correlation is not surprising as studies on the relationship between structural anisotropy and rheology are not confined to colloidal gels. Many studies on the colloidal suspension, such as colloidal glasses, have focused on the relationship between structural anisotropy and rheology [18,21-23]. In a recent study, a quantitative relationship between flow-induced anisotropic structure and rheological behavior was established via the stress-SANS rule for colloidal suspensions [24]. Furthermore, in many studies on soft colloidal dispersions, such as polymer-like micelles [25,26], structural anisotropy has been associated with non-linear rheology by computing the stress with the stress-SANS rule, which is comparable to the stress-optic rule. However, questions remain when applying such relationships to colloidal gels due to the distinct bond-breakage that is characteristic in such systems and which is not explicitly incorporated into stress-optical and stress-SANS relationships.

Although structural anisotropy in shearing colloidal gels has been well documented [27,28], there still is a lack of understanding on the mechanism leading to structural anisotropy. Especially, when compared with the structural anisotropy evident along compressional and extensional directions, there is a relatively limited understanding on the origin of structural anisotropy along the vorticity direction. Recently, Cheng *et al.* [29] elucidated the role of hydrodynamic interaction and confinement in formation of anisotropic structure along the vorticity direction. However, the influence of surface-mediated attractive interactions, which dominate many colloidal gel systems, still remains an unsolved problem. In addition, the coupling between structural anisotropy and rheology has not been quantified.

As a continuation of our previous work in which the microstructural evolution of colloidal gel under startup shear is analyzed from three points of view (cluster length scale, local length scale,

anisotropy) [4], the purpose of the present work is to quantitatively investigate the origin of shear-induced structural anisotropy and its correlation with rheology using the simulation tools developed in this prior work. The structural evolution of a model colloidal gel at an intermediate volume fraction (20%) is studied under startup of shear flow. In real space, the shear-induced structural anisotropy is investigated by computing pair distribution functions. A spherical harmonic expansion of the pair distribution function provides quantitative analysis of structural changes. In reciprocal space, we compute the structure factor, which can be directly compared to the experimental scattering measurements. This structural anisotropy is correlated to the rheological behavior via a stress-SANS rule. In this process, by explicitly considering bond rupture and creation within the shearing colloidal gel, the stress-SANS rule is modified to accurately relate the structural anisotropy to non-linear rheology.

## II. Simulation details

### A. Particle interaction

A recent study of colloidal micromechanics using laser tweezers quantified the near contact interactions of colloidal particles [30]. The importance of non-central forces, such as particle adhesion and surface roughness, on gel micromechanics was highlighted. Surface contact interactions between particles is manifested as bending rigidity for chains of colloidal aggregates. Such bonds between particles can support substantial torque, which is important for gel rheology. This physics cannot be described by conventional Brownian dynamics simulation methods, which assume smooth, ideal spherical particles with centro-symmetric interactions. We have developed a Brownian dynamics simulation method that incorporates a model for surface bonding, which describes the rotational motion and restricts the angular reorganization with reversible and flexible bonds between particle surfaces, and thereby, includes the non-central interaction physics of colloidal gels. This simulation method has successfully reproduced many experimentally observed structural changes and rheological behaviors of colloidal gels [4,5,31]. The complete algorithmic details concerning the simulation methods are documented in detail elsewhere [4,32] and here, only details specific to this simulation and particle interactions are presented for brevity. It is important to recognize that the non-central forces included in this model distinguish our simulation method from the majority of published studies, which only include central forces. These non-central forces are important to capture gel

rheology and structure under flow, as will be shown in the following.

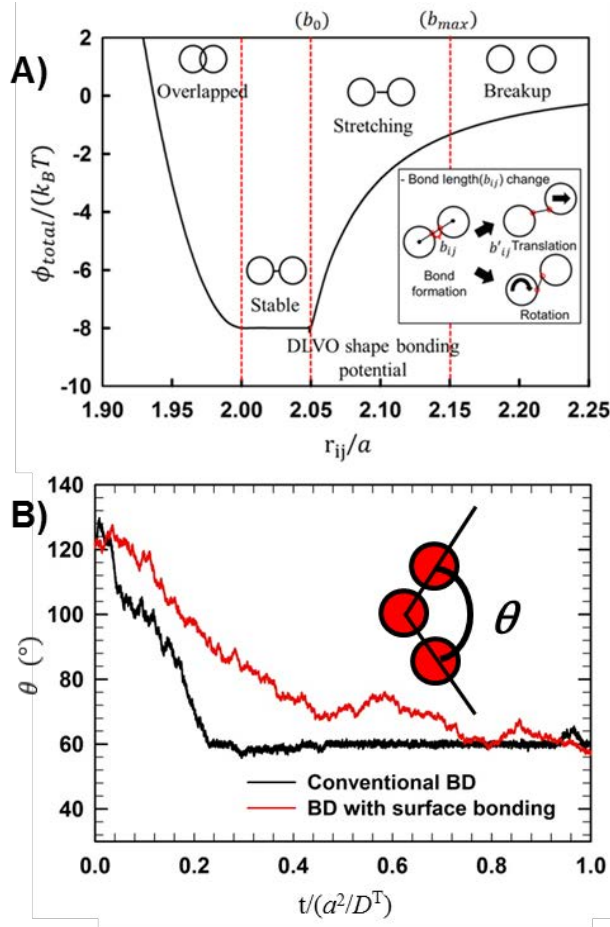


**Fig. 1. A)** Pair interaction potential for a co-linear extension, which consists of core potential ( $\phi_C$ , for  $r_{ij} < 2a$ ), bonding potential ( $\phi_B$ , for  $2a \leq r_{ij} \leq 2a + b_{\max}$ ) and non-bonded long range potential ( $\phi_N$ , for  $2a + b_{\max} < r_{ij}$ ). The bonding potential,  $\phi_B$  and non-bonded long range potential,  $\phi_N$  are supposed to have a DLVO shape potential ( $a = 1 \mu\text{m}$ ,  $A = 3.2 \times 10^{-20} \text{J}$ ,  $\varepsilon = 81 \varepsilon_0 \text{Fm}^{-1}$ ,  $\psi = 4 \text{mV}$ ,  $\kappa = 5 \times 10^7 \text{m}^{-1}$ ). The inset shows schematic illustrations of bond formation, translational motion and rotational motion of the particles. **B)** Change of the angle between three particles, which were initially placed to form  $120^\circ$ , is demonstrated for standard Brownian dynamics simulations and simulations including a surface bond potential. The results represent averages over 20 different simulations with different random motion.

This work explores weakly attractive colloidal gel at low volume fraction. The simulation system consists of 10,648 particles which are placed in a three dimensional cubic, periodic simulation cell (20%

volume fraction). The Lee-Edwards boundary condition is introduced in all three orthogonal directions. The dynamics are governed by the Langevin equation [33] according to which, the position of each particle is updated. The governing equations are formulated in respect of dimensionless parameters. The Brownian motion of the particles is described by stochastic displacement caused by the corresponding Gaussian random force. The length and energy are scaled with the radius ( $a$ ) of the particle and the thermal energy ( $k_B T$ ) respectively. The time is scaled by the characteristic time

$\tau_B = \frac{a^2}{D^T}$ , where  $D^T$  is the translational diffusion coefficient of the particle in infinitely dilute

solution. The force of the imposed shear flow acting on a particle pair,  $6\pi\eta a^2 \dot{\gamma}$ , is compared to thermal restoring force,  $k_B T / a$ , defining the Peclet number as  $Pe = \dot{\gamma} a^2 / D^T$ . Hydrodynamic interactions between the particles are not considered and hydrodynamic force is assumed to be the Stokesian drag force. It should be noted that Brownian dynamic simulations without hydrodynamic interactions have described the equilibrium properties of some colloidal gel systems [3,16]. It is important, however, to note that hydrodynamic interactions between particles can affect the microstructure of colloidal gels by altering their formation kinetics [34,35]. Therefore, the results shown herein should be viewed within the assumption of neglect of hydrodynamic interactions, which may play a role in both the gel formation and gel flow under shear.

In this work, particles interact through three potentials; core potential ( $\phi_C$ ), bonding potential ( $\phi_B$ ), and non-bonded long-range potential ( $\phi_N$ ):

$$\begin{aligned} \phi_C(r_{ij}) &= \frac{1}{2} K (2a - r_{ij})^2, \quad r_{ij} < 2a \\ &= 0, \quad r_{ij} \geq 2a \end{aligned} \quad (1)$$

The core potential is given by a steep repulsive potential with the potential energy parameter,  $K=4000$ , where  $r_{ij} = |\mathbf{r}_i - \mathbf{r}_j|$  indicates the inter-particle distance. In the Brownian dynamics simulation with surface bonding, a bond is formed on the particle surface when two particles approach each other within a critical separation ( $r_{ij} < 2.15a$ ). The bond formed on the particle surface induces force and torque, which results in translational and rotational relative motion of the particles. We assume that the bond has a potential of DLVO type given by:

$$\phi_{DLVO}(r_{ij}) = \phi_{vdW}(r_{ij}) + \phi_{el}(r_{ij}) \quad (2)$$

$$\phi_{vdW}(r_{ij}) = -\frac{A}{6} \left[ \frac{2a^2}{r_{ij}^2 - 4a^2} + \frac{2a^2}{r_{ij}^2} + \ln \left( \frac{r_{ij}^2 - 4a^2}{r_{ij}^2} \right) \right] \quad (3)$$

$$\varphi_{el}(r_{ij}) = \frac{\varepsilon a \psi^2}{2} \left[ \ln \left( 1 + \exp \left( -\kappa (r_{ij} - 2a) \right) \right) \right] \quad (4)$$

where  $A, \varepsilon, \psi$ , and  $\kappa$  represent the Hamaker constant, the dielectric constant of solvent, the surface potential of the particle, and the Debye screening length, respectively. In accordance with the bond length between the particle surfaces,  $b_{ij}$ , the bonding potential is distinguished into two parts:

$$\begin{aligned} \phi_B(b_{ij}) &= \varphi_{DLVO}(b_0 + 2a), \quad b_0 \geq b_{ij} \\ &= \varphi_{DLVO}(b_{ij} + 2a), \quad b_{\max} \geq b_{ij} > b_0 \end{aligned} \quad (5)$$

In case the bond length is shorter than  $b_0$ , the bonding potential is set to a constant value of  $\varphi_{DLVO}(b_0 + 2a)$  to describe the stable region where there is no attractive force. For the bonds with the bond length longer than  $b_0$  and shorter than the maximum bond length,  $b_{\max}$ , we assume the bonding potential as a spring with a DLVO potential. When the particles get detached from each other, the bond length exceeds the maximum bond length and the bond breaks. After breaking, the non-bonded long range interaction  $\phi_N(r_{ij})$  describes the particle interactions in the absence of non-central surface bonding interactions. This central inter-particle potential is set as the DLVO potential as follows:

$$\phi_N(r_{ij}) = \varphi_{DLVO}(r_{ij}) \quad (6)$$

The three potentials come together to create the total interparticle potential, which is a function of the inter-particle distance,  $r_{ij}$ , and bond length,  $b_{ij}$ , as follows:

$$\begin{aligned} \phi_{total}(r_{ij}, b_{ij}) &= \phi_C(r_{ij}) + \phi_B(b_{ij}) + \phi_N(r_{ij}) \\ \mathbf{F}_{ij} &= -\nabla \phi_{total}(r_{ij}, b_{ij}) \end{aligned} \quad (7)$$

By calculating the gradient of the total inter-particle potential, we can get the total inter-particle force ( $\mathbf{F}_{ij}$ ), which induces the translational and rotational motion of the particles. In Fig. 1 (A), the total pair interaction potential is plotted for a collinear extension case, in which the bond length ( $b_{ij}$ ) coincides with the surface separation,  $r_{ij} - 2a$ .

Figure. 1 (B) shows the difference between a conventional Brownian dynamics simulation and Brownian dynamics simulation with surface bonding concept. It is illustrated in Fig.1 (B) that the

angle between three particles, which is initially  $120^\circ$ , changes over time. In both case of conventional Brownian dynamics and Brownian dynamics with surface bonding, the angle between the three particles converges to  $60^\circ$ , so as to form the thermodynamically stable configuration. However, in the case of Brownian dynamics simulation with surface bonding model, it takes longer to reach the most stable state than the conventional Brownian dynamics simulation. This difference shows the role of the surface bond, which not only acts to bring particles together, but also to restrict the relative angular motion.

## B. Structure analysis method

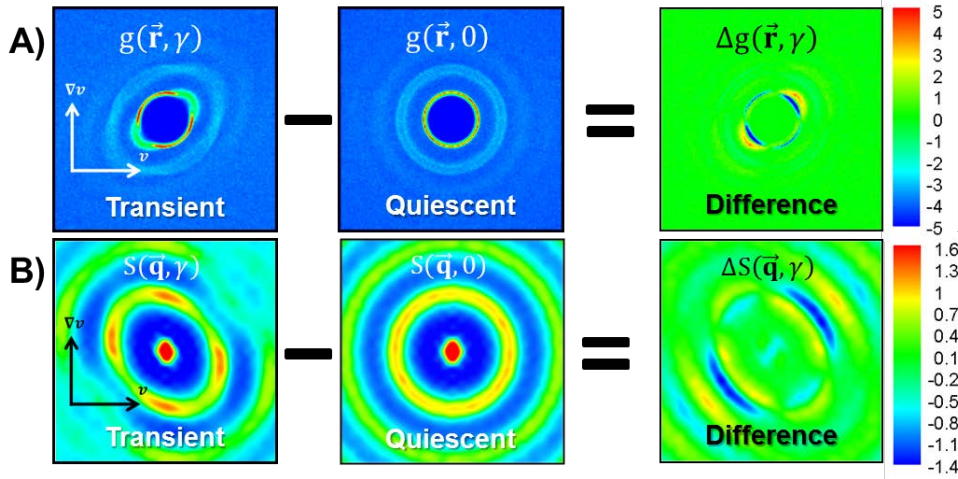


**Fig. 2.** Calculation of pair distribution function difference,  $\Delta g(\mathbf{r}, \gamma=1)$  and structure factor difference,  $\Delta S(\mathbf{q}, \gamma=1)$ .

Structural changes in the colloidal gel are studied by analyzing the pair distribution function,  $g(\mathbf{r}, \gamma)$ , and structure factor,  $S(\mathbf{q}, \gamma)$ . The pair distribution function and the structure factor measure the normalized probability of finding a particle center at relative position of  $\mathbf{r}$  in real space and  $\mathbf{q}$  in reciprocal space at strain  $\gamma$ . Here, the pair distribution function and the structure factor are given by:

$$g(\mathbf{r}, \gamma) = \frac{V}{N^2} \left\langle \sum_i \sum_{j \neq i} \delta(\mathbf{r} - \mathbf{r}_{ij}) \right\rangle \quad \text{at strain } \gamma \quad (8)$$

$$S(\mathbf{q}, \gamma) = 1 + \frac{V}{N} \left\langle \sum_i \sum_{j \neq i} \exp(-i\mathbf{q} \cdot \mathbf{r}_{ij}) \right\rangle \text{ at strain } \gamma \quad (9)$$

where  $N, V, \mathbf{q}$  represent the number of the particles, the volume of the simulation box and the wave vector, respectively. To quantify the structural change during startup shear flow quantitatively, we examine both the pair distribution function and the structure factor as differences between a transient state ( $\gamma \neq 0$ ) and quiescent state ( $\gamma = 0$ ). Figure. 2 demonstrates the calculation of the pair distribution function difference and the structure factor difference. The second figures in Fig. 2(A) and Fig. 2(B) demonstrate the pair distribution function  $g(\mathbf{r}, 0)$  and the structure factor  $S(\mathbf{q}, 0)$  in the quiescent state. In the quiescent state, both the pair distribution function and structure factor are isotropic as expected for liquid or a gel quenched from a liquid structure, but not necessarily for a gel formed by shearing, such as typical for depletion gels. The first figures of Fig. 2(A) and Fig. 2(B) display pair distribution function,  $g(\mathbf{r}, \gamma)$ , and structure factor,  $S(\mathbf{q}, \gamma)$ , calculated for a transient state ( $\gamma = 1$ ). In this transient state, distortions and intensity changes are evident that can be attributed to the shear-induced structural change. The last figures of Fig. 2(A) and Fig. 2(B) demonstrate the pair distribution function difference,  $\Delta g(\mathbf{r}, \gamma)$ , and structure factor difference,  $\Delta S(\mathbf{q}, \gamma)$ , which are defined as:

$$\Delta g(\mathbf{r}, \gamma) = g(\mathbf{r}, \gamma) - g(\mathbf{r}, 0) \quad (10)$$

$$\Delta S(\mathbf{q}, \gamma) = S(\mathbf{q}, \gamma) - S(\mathbf{q}, 0) \quad (11)$$

The differences,  $\Delta g(\mathbf{r}, \gamma)$  and  $\Delta S(\mathbf{q}, \gamma)$ , effectively capture the structural changes relative to the initial, quiescent state, making it easier to distinguish shear-induced structure formation and breakup.

In Fig. 2, it is shown that the pair distribution function and the structure factor, which are isotropic at quiescent state, demonstrate anisotropy under shear flow due to shear-induced non-equilibrium structure. To quantify this structural anisotropy, we follow the literature and expanded the pair distribution function  $g(\mathbf{r}, \gamma)$  in spherical harmonics [36,37]. The pair distribution function can be expanded in terms of spherical harmonics  $Y_{lm}(\hat{\mathbf{r}})$  as:

$$g(\mathbf{r}) = g_s + \sum_l \sum_{m=-l}^l g_{lm}(r) Y_{lm}(\hat{\mathbf{r}}) \quad (12)$$

The scalar contribution  $\mathbf{g}_S(r)$  is: `

$$\mathbf{g}_S(r) = \frac{1}{4\pi} \int \mathbf{g}(\mathbf{r}) d\hat{\mathbf{r}} \quad (13)$$

The expansion coefficients are given by:

$$\mathbf{g}_{lm}(r) = \int Y_{lm}(\hat{\mathbf{r}}) \mathbf{g}(\mathbf{r}) d\hat{\mathbf{r}} \quad (14)$$

Here,  $\hat{\mathbf{r}}$  denotes  $\hat{\mathbf{r}}/r$ .

For a fluid subjected to plane Couette flow, using Cartesian irreducible tensors, this spherical harmonic expansion can be further simplified as follows: [38,39]

$$\begin{aligned} \mathbf{g}(\mathbf{r}) &= \mathbf{g}_S(r) + \sum_l \sum_k \mathbf{g}_k^{(l)} X_k^{(l)}(\hat{\mathbf{r}}) \\ &= \mathbf{g}_S(r) + \mathbf{g}_0^{(2)} X_0^{(2)} + \mathbf{g}_1^{(2)} X_1^{(2)} + \mathbf{g}_2^{(2)} X_2^{(2)} + \mathbf{g}_0^{(4)} X_0^{(4)} + \mathbf{g}_1^{(4)} X_1^{(4)} + \end{aligned} \quad (15)$$

where  $X_k^{(l)}(\hat{\mathbf{r}})$  is given as:

$$X_0^{(2)} = \hat{z}^2 - \frac{1}{3}, X_1^{(2)} = \frac{1}{2}(\hat{x}^2 - \hat{y}^2), X_2^{(2)} = \hat{x}\hat{y} \quad (16)$$

for structure up to rank 2. In Eq. 16,  $\hat{x}, \hat{y}, \hat{z}$  are the components of  $\hat{\mathbf{r}}$ . The  $X_k^{(l)}$  terms are closely connected to the spherical harmonics terms  $Y_{lm}$ . In the case of even  $k$ ,  $X_k^{(l)}$  is proportional to  $\text{Im}Y_{lk}$  and for odd  $k$ ,  $X_k^{(l)}$  is proportional to  $\text{Re}Y_{lk+1}$ . For zero  $k$ ,  $X_k^{(l)}$  is proportional to  $Y_{l0}$ . The expansion coefficient  $\mathbf{g}_k^{(l)}$  is:

$$\mathbf{g}_k^{(l)}(r) = (\xi_l)^2 C_k^{(l)} \left( \frac{1}{4\pi} \right) \int X_k^{(l)}(\hat{\mathbf{r}}) \mathbf{g}(\mathbf{r}) d\hat{\mathbf{r}} \quad (17)$$

where  $\xi_l$  and  $C_k^{(l)}$  are:

$$\begin{aligned} \xi_l &= \{(2l+1)!!/l!\}^{1/2} \\ C_0^{(2)} &= \frac{3}{2}, C_1^{(2)} = C_2^{(2)} = 2 \end{aligned} \quad (18)$$

Here the double factorial (!! ) is:

$$(2l+1)!! = \prod_{k=1}^{(l+1)} (2k-1) = (2l+1)(2l-1)(2l-3) \dots 1 \quad (19)$$

By comparing the expansion coefficients  $\mathbf{g}_k^{(l)}$ , which indicates the degree of the structural anisotropy related to each Cartesian irreducible tensor terms  $X_k^{(l)}$ , the shear-induced anisotropic structure of the colloidal gel under startup shear can be quantified.

For the structure factor,  $\mathbf{S}(\mathbf{q}, \gamma)$ , the degree of structural anisotropy is also characterized by the alignment factor,  $A_f$  [40,41] defined as:

$$A_f = \frac{\int_0^{2\pi} I(q^*, \phi, \gamma) \cos(2(\phi - \phi_0)) d\phi}{\int_0^{2\pi} I(q^*, \phi, \gamma) d\phi} \quad (20)$$

where  $I(q^*, \phi, \gamma)$  denotes the angular scattering intensity averaged over a  $q$ -range of  $q^*$  ( $2.8a^{-1} \leq q \leq 3.6a^{-1}$ ) corresponding to the local structure of length scale  $\sim 2a$ , i.e., nearest neighbors. Here,  $\phi$  and  $\phi_0$  are the azimuthal angle relative to x-axis and the average orientation of the local structure, which is given by the minimum of  $I(q^*, \phi, \gamma)$ . The alignment factor  $A_f$ , which is commonly used in scattering data analysis, indicates the degree of alignment of the structure about  $\phi_0$ , and has been typically used for studying polymers and polymer-like micelles, but has more recently been adopted for studying colloidal gels [8,13]. In a simplified scattering analysis, the scattering intensity  $I(\vec{\mathbf{q}}, \gamma)$  is given by:

$$I(\mathbf{q}, \gamma) = p(\mathbf{q}) \times \mathbf{S}(\mathbf{q}, \gamma) \quad (21)$$

where  $p$  is the form factor of the particles. For gels of nonbreaking colloidal spheres, such as considered here, the particle form factor remains unchanged by the shear flow and structure factor  $\mathbf{S}(\mathbf{q}, \gamma)$  is used to calculate the alignment factor,  $A_f$ , instead of the scattering intensity  $I(\mathbf{q}, \gamma)$ .

### III. Results and discussion

#### A. Rheology and structural change under shear flow

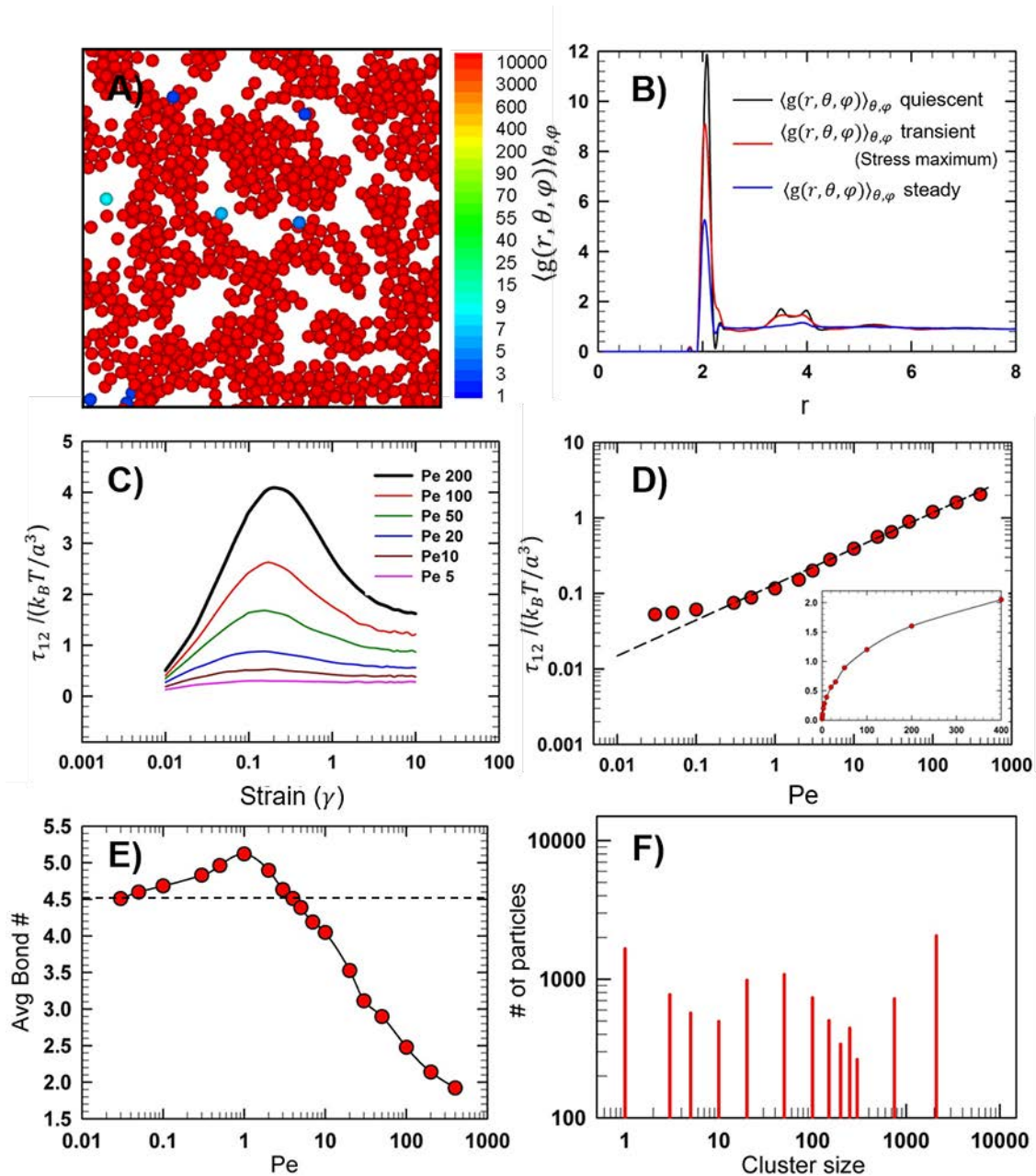


**Fig. 3.** (A) Gel structure in the quiescent state. The image shows particles at the center of the simulation box in a slice with a thickness of  $4a$ . The color indicates the size of cluster to which the particles belong. (B) Angular averaged pair distribution function  $\langle g(r, \theta, \varphi) \rangle_{\theta, \varphi}$  (radial distribution function) of the colloidal gel in a quiescent state, transient state, and steady state under steady shear flow of Pe 200. (C) Stress-overshoot behavior of the colloidal gel. In this work, Pe 200 case (thick black curve) is mainly studied. (D) Flow curve of the colloidal gel. Inset shows the result on a linear

scale. **(E)** Average bond number at steady state at various Pe values. Dashed line denotes the average bond number in the quiescent state. **(F)** Particle number distribution according to the cluster size at steady state of Pe 200.

Figure. 3 displays rheological and structural information on the model colloidal gel system. Figure. 3(A) shows the initial gel structure in the quiescent state, where the gel is quenched from a liquid structure. Initially, 99% of the total particles aggregated to yield a percolated, network structure. Note that the presence of non-central forces, i.e., surface bonds, prevents large-scale phase separation (on the time scales of interest) as is typically observed in BD simulation of colloids with depletion interactions. This enables us to use a reasonable simulation size to study our system, whereas or order  $10^6$  particle are required for the depletion systems [42]. Under startup of shear flow, the colloidal gel experiences various structural changes. The angular averaged pair distribution function  $\langle g(r, \theta, \varphi) \rangle_{\theta, \varphi}$  in Fig. 3(B), demonstrates some of these structural changes. Under shear flow, as strain increases the first maximum peak in  $\langle g(r, \theta, \varphi) \rangle_{\theta, \varphi}$  decreases. Considering that the first maximum peak, which is called as the nearest neighbor peak, corresponds to a length scale of a particle size, this angular averaged pair distribution function change under shear flow can be recognized as a shear-induced reduction in the local organization in the microstructure. This shear-induced structural change is also evident as a decrease in second maximum peak, which is referred to as the second nearest neighbor peak.

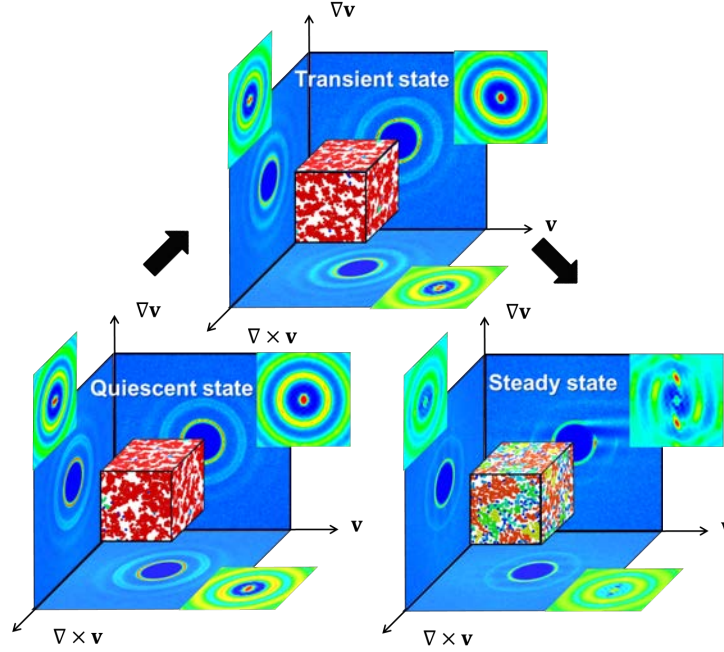
This apparently monotonic structural change manifests itself as a non-linear rheological response. In Fig. 3(C), the stress growth under startup shear is shown as a function of strain. As the strain increases, the stress increases up to a maximum and then decreases to a steady value, signifying attainment of a rheological steady state flow. This stress overshoot increases with Pe while the strain at maximum stress is invariant. This stress-overshoot behavior has been studied in terms of structural rupture of colloidal gels [4], which is represented by the decrease in the maximum peaks of  $\langle g(r, \theta, \varphi) \rangle_{\theta, \varphi}$  in this work. In the beginning of startup shear, the colloidal gel experiences deformation but maintains the network structure. During this initial deformation, the stress accumulates in the network structure, which corresponds to linear rheological behavior. However, as strain increases further, the stress-bearing network structure is ruptured and the colloidal gel shows a commensurate decrease in stress.

In Fig. 3(D), steady shear measurements demonstrate the shear thinning behavior of the colloidal gel. At low Pe, where the Brownian motion can relax shear-induced deformation, the colloidal gel

maintains its structure. Therefore, the colloidal gel shows high viscosity. However, as  $Pe$  is increased, shear flow more strongly influences the colloidal gel structure. Faster shear flow hinders the relaxation of the colloidal gel structure by bond elasticity and Brownian motion, and induces rupture of the colloidal gel structure. This leads to a decrease of the viscosity. Fig. 3(D) shows the flow curve on a log scale. This result is in qualitative agreement with the prediction of models such as the soft glassy material rheology (SGR) model [43-45], which has been proposed to model soft materials, such as colloidal glasses [46,47] and a colloidal gel [48]. In Fig. 3(D), the steady shear stress and  $Pe$  demonstrate power-law behavior with exponent 0.48, which corresponds to the theoretical prediction of the SGR model, 0.5.

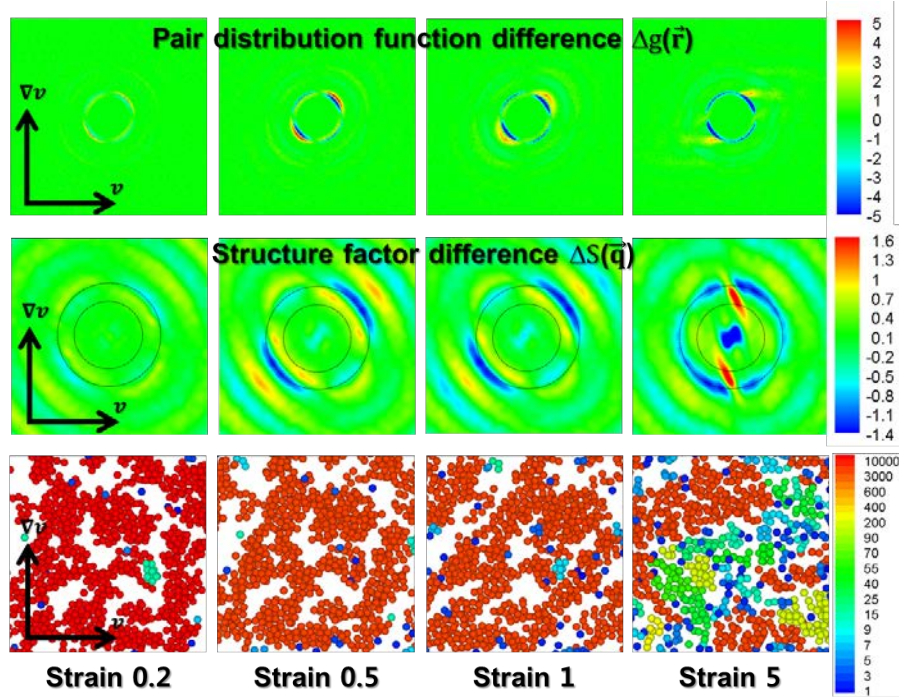
Figure. 3(E) shows change in average bond number at steady state over  $Pe$ . At low  $Pe$ , shear flow densifies the colloidal gel structure, which is represented by slight increase in average bond number. This result corresponds to previous works [16] where shear flow makes clusters more dense at low  $Pe$ . In Fig. 3(F), particle number distribution according to the cluster size at steady state of  $Pe$  200 is displayed. At the shear flow condition that corresponds to inverse Bingham number  $M'$  [13] or  $Pe_{dep}$  [16] of 1, the network structure of colloidal gel is ruptured to small clusters and individual particles.

## B. Structural anisotropy under startup shear



**Fig. 4.** Diagrams of 3D colloidal gel structure under flow startup. The simulated colloidal gel configurations are analyzed through pair distribution function (large plane with majority blue color) and structure factor (small plane with majority green color). The pair distribution function and structure factor are projected for the three perpendicular planes of velocity-gradient ( $\mathbf{v} - \nabla\mathbf{v}$ ), velocity-vorticity ( $\mathbf{v} - \nabla \times \mathbf{v}$ ), and gradient-vorticity ( $\nabla\mathbf{v} - \nabla \times \mathbf{v}$ ).

Next, we investigate the structural anisotropy induced by shear startup by considering the anisotropy in the pair distribution function and the structure factor. Figure. 4 shows representative plots of the structural anisotropy evident in the real and scattering space representations, along with a representative snapshot of the simulation itself. From the simulation particle coordinates, the pair distribution function and the structure factor were calculated in three orthogonal planes of velocity-gradient, velocity-vorticity, and gradient-vorticity. By investigating changes in the pair distribution function change and the structure factor in the transient state, the development of the structural anisotropy of the colloidal gel under startup shear has been analyzed and correlated to the relevant stress responses.

1) Velocity-gradient ( $\mathbf{v} - \nabla\mathbf{v}$ ) plane

**Fig. 5.** Pair distribution function difference ( $\Delta g(\mathbf{r}, \gamma) = g(\mathbf{r}, \gamma) - g(\mathbf{r}, 0)$ ) (top row) and structure factor difference ( $\Delta S(\mathbf{q}, \gamma) = S(\mathbf{q}, \gamma) - S(\mathbf{q}, 0)$ ) (middle row) in the velocity ( $\mathbf{v}$ )–gradient ( $\nabla\mathbf{v}$ ) plane. Snapshots of the particle configuration (bottom row). The images show the particles in the velocity-gradient plane sliced with a thickness of  $4a$ . The color indicates the size of the cluster to which the particles belong. The black circles in the structure factor difference indicate the  $q$  range ( $q^*$ ) corresponding to the nearest neighbor structure.

The top row in the Fig. 5 shows the pair distribution function difference,  $\Delta g$ , in the velocity ( $\mathbf{v}$ )–gradient ( $\nabla\mathbf{v}$ ) plane during the startup shear. As strain increases, the innermost ring of the pair distribution function difference, which corresponds to nearest neighbor structure, shows a strong decrease along the extensional axis of shear. In contrast, along the compressional axis of shear, a relatively minor perturbation of the pair distribution function is observed. The structure factor shows this structural anisotropy along the compressional axis as well, as evident from the middle row of Fig. 5, which plots the structure factor difference  $\Delta S$  in velocity ( $\mathbf{v}$ )–gradient ( $\nabla\mathbf{v}$ ) plane. Between

the black circles, which delineate  $q$  range corresponding to the nearest neighbor structure, the structure factor shows an increase along the extensional axis and a decrease along the compressional axis. Considering the inherent inverse relationship between reciprocal space and real space, the structure factor, which analyzes the microstructure in reciprocal space, shows patterns that corresponds to  $90^\circ$  rotation of the pair distribution function. Therefore, the increase in the structure factor along the extensional axis can be correlated to the microstructure increasing along the compressional axis in real space. These simulation results are qualitatively consistent with experimental observations on colloidal gels under shear flow [13].

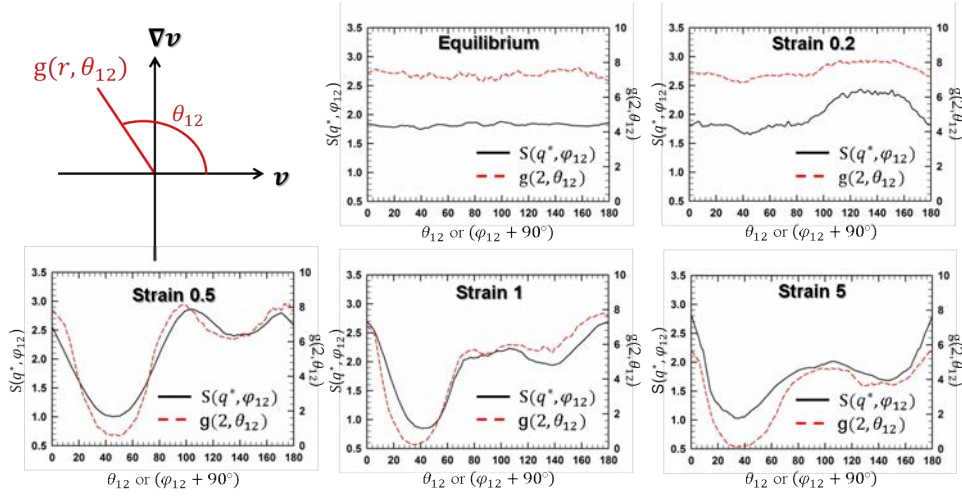


**Fig. 6.** Angular variation of the pair distribution function  $g(r, \theta_{12})$  and the structure factor  $S(q, \varphi_{12} + 90^\circ)$  over the entire contact surface ( $r=2, q=q^*$ ) in the velocity ( $\mathbf{v}$ )-gradient ( $\nabla\mathbf{v}$ ) plane.

The structural anisotropy can be analyzed quantitatively by investigating angular variation of the pair distribution function and the structure factor over specific radial slices in the 2D projections of the structure ( $r=2, q=q^*$ ). Figure. 6 shows the angular variation of these pair distribution function  $g(2, \theta_{12})$  and the structure factor  $S(q^*, \varphi_{12} + 90^\circ)$ . Here, the abscissa of the structure factor is given as a function of  $\varphi_{12} + 90^\circ$  to account for the inverse relationship between reciprocal space and real space. This corresponds to the rotated scattering patterns as presented in this manuscript. (The analysis of angular variation in the velocity ( $\mathbf{v}$ )-vorticity ( $\nabla \times \mathbf{v}$ ) plane and gradient ( $\nabla\mathbf{v}$ )-vorticity ( $\nabla \times \mathbf{v}$ ) plane employ the same notation.) At the equilibrium state of strain 0,

both the pair distribution function and the structure factor demonstrate an isotropic structure, which is described by flat curves with no angular dependence. As the strain increase from strain 0 to strain 0.2 the pair distribution function becomes anisotropic and angular dependence on the length scale of the nearest neighbor are evident. The angular variation at strain 0.2 shows an increase in the pair distribution function and the structure factor along the compressional axis direction ( $\theta_{12} = \varphi_{12} + 90 = 135$ ). On the other hand, no significant change is observed along the extensional axis direction ( $\theta_{12} = \varphi_{12} + 90 = 45$ ). As strain increases to 0.5, a rapid decrease in the pair distribution function and the structure factor is observed in the extensional axis direction ( $\theta_{12} = \varphi_{12} + 90 = 45$ ). Meanwhile, the pair distribution function and the structure factor in the compressional axis do not change.

As strain increases further and steady state flow is achieved (strain 5), the colloidal gel shows an overall decrease in the pair distribution function and the structure factor, as shown in Fig 3. Importantly, the pair distribution function and the structure factor show strong anisotropy on length scales corresponding to nearest neighbors. This structural anisotropy is a critically important aspect of the evolution of colloidal gels under startup shear [4]. Initially, when shear flow is imposed, the colloidal gel deformation is largely affine. The slight increase in the pair distribution function and the structure factor along the compressional axis direction at strain 0.2 indicates that the initial structural change of the colloidal gel takes the form of compression. With increasing strain, the colloidal gel structure undergoes a break-up along the extensional axis. This break-up leads to a reduction in the number of neighboring particles along the extensional direction, while the microstructure along the compressional axis is maintained (strain 0.5). As strain increases further, the colloidal gel network structure undergoes rotational motion toward the flow direction and ruptures into several clusters and flocs as shown in Fig. 5 (strain 5). The rotation and breakup of the overall colloidal gel structure bring about the overall decrease in the pair distribution function and the structure factor. By this process, despite the overall decrease of the pair distribution function and the structure factor, the break-up along the extensional axis and the shear-induced aggregation along the compressional axis generate significant structural anisotropy.

At steady state flow (strain 5), where the colloidal gel is ruptured into several clusters and flocs, the colloidal gel shows the structural anisotropy qualitatively similar to that reported for hard sphere colloidal suspensions [17,24]. In addition to the structural anisotropy along the compressional axis, the ruptured colloidal gel shows some propensity for “string-like” organization along the flow direction, which is represented by the increase of the structure factor along the gradient axis in Fig. 5 (strain 5). The alignment along the flow direction has been observed in previous theoretical [17,49]

and experimental works with hard sphere system [24,50]. Besides the alignment along the flow direction, the overall angular distribution of the ruptured colloidal gel in Fig. 6 (strain 5) shows similarities to the hard sphere system.

The spherical harmonics expansion of the pair distribution function  $g(\mathbf{r})$  provides more quantitative metrics for the structural anisotropy. In Fig. 7(A), the spherical harmonic coefficient  $g_2^{(2)}(r)$ , which denotes the intensity of spherical harmonic term  $X_2^{(2)}$ , is displayed for various strains. Initially, at strain 0,  $g_2^{(2)}(r)$  is described by a flat curve, which corresponds with the isotropic colloidal gel structure at equilibrium state. As strain increases, the result shows two peaks at  $r \cong 2$  and in between 2 and 2.15. At  $r \cong 2$ , the peak shows minima of negative value. Because  $X_2^{(2)}$  describes an anisotropic structure with symmetries along the extensional and compressional axes as shown in the inset of the Fig. 7(A), the negative value of  $g_2^{(2)}(r)$  can be interpreted as a result of anisotropic structure buildup along the compressional direction. On the other hand, in between 2 and 2.15,  $g_2^{(2)}(r)$  demonstrates maxima with positive value, which indicates an anisotropic increase in structure along the extensional axis. These different structural anisotropies with varying particle separation distance  $r$  are associated with specifics of particle motion in the gel under shear flow. Under shear flow, particles approach to each other along the compressional axis. At the same time, particles are convected away along the extensional axis. Therefore, at  $r \cong 2$ , where particle surfaces are convected into contact, the colloidal gel shows structural anisotropy along the compressional axis with negative  $g_2^{(2)}(r)$ . On the other hand, in between 2 and 2.15, structural anisotropy along the extensional axis is observed. This is because the particle bonds are stretched to a value in between 2 (particle surface contact) and 2.15 (maximum stretching) by shear flow. As strain increases, lower peak values are observed, which is ascribed to the rupture of the colloidal gel structure, such that fewer neighboring particles are evident at this separation distance along the extensional axis.

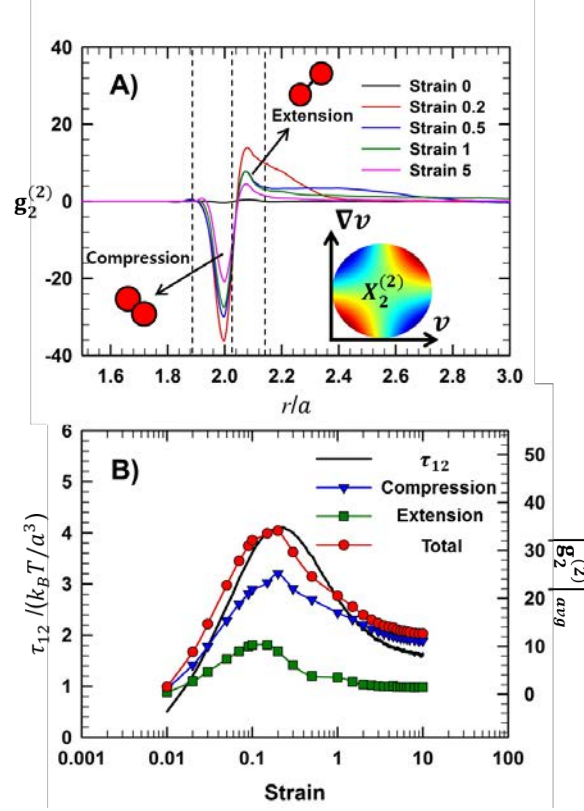


**Fig. 7.** **A)** Spherical harmonic function  $X_2^{(2)}$  (inset) and coefficient  $g_2^{(2)}$ . Dotted lines denote the compression part and the extension part. **B)** Absolute value of  $g_2^{(2)}$  coefficient averaged over compressional part (blue down triangle) and extensional part (green square) and sum (red circle) as a function of strain ( $\gamma$ ). Black solid line shows shear stress response  $\tau_{12}$  of the colloidal gel.

Unlike the overall averaged microstructure, the structural anisotropy in velocity ( $\mathbf{v}$ )-gradient ( $\nabla\mathbf{v}$ ) plane shows a strong correlation to the shear stress responses. In previous work [36], it has been shown that the shear stress  $\tau_{12}$  for molecular systems interacting with a simple centrosymmetric potential can be given as:

$$\tau_{12} = -\frac{2}{15}\pi\rho^2\int_0^\infty r^3 g_2^{(2)}\left(\frac{d\phi}{dr}\right)dr \quad (22)$$

where  $\rho$  is the particle number density and  $\left(\frac{d\phi}{dr}\right)$  is the derivative of interparticle potential, which is equivalent to inter-particle force. Even though Eq. 22 provides a quantitative relationship between

$g_2^{(2)}$  and the shear stress  $\tau_{12}$ , it is not automatically applicable to our work, where the interparticle potential is given by a function of the bond length between the particle surfaces ( $b$ ) as well as the interparticle distance ( $r$ ). To test this relationship, we compared the  $g_2^{(2)}$  coefficient to the shear stress  $\tau_{12}$ . To compare  $g_2^{(2)}$  to  $\tau_{12}$ ,  $g_2^{(2)}$  was averaged in compressional part and extensional part, separately. Because both of compressional part (negative  $g_2^{(2)}$  and positive  $\left(\frac{d\phi}{dr}\right)$  due to repulsive force by surface potential) and extensional part (positive  $g_2^{(2)}$  and negative  $\left(\frac{d\phi}{dr}\right)$  due to attractive force by bonding potential) contribute positively to  $\tau_{12}$ , we compared the sum of  $\left|g_2^{(2)}\right|_{avg}$  in the compressional part and extensional part to  $\tau_{12}$ . Fig. 7(B) shows the evolution of  $\left|g_2^{(2)}\right|_{avg}$  and shear stress ( $\tau_{12}$ ) as a function of strain ( $\gamma$ ). In addition to the stress overshoot behavior,  $\left|g_2^{(2)}\right|_{avg}$  of the compressional part, the extensional part, and sum of them all show overshoot behavior with strain. The overshoot behavior of the sum of  $\left|g_2^{(2)}\right|_{avg}$  corresponds well with that of the stress curve, importantly showing the coincidence of the maxima of  $\left|g_2^{(2)}\right|_{avg}$  and  $\tau_{12}$ .

## 2) Velocity-vorticity ( $\mathbf{v} - \nabla \times \mathbf{v}$ ) plane

The top row of Fig. 8 shows the pair distribution function difference,  $\Delta g$ , in the velocity ( $\mathbf{v}$ )–vorticity ( $\nabla \times \mathbf{v}$ ) plane under the startup shear. As strain increases, the innermost ring of the pair distribution function shows a strong decrease along the velocity direction and a relatively slight decrease along the vorticity direction. The pair distribution function difference shows the expected structural anisotropy along the vorticity axis. The structural anisotropy along the vorticity axis is also observed in the structure factor difference,  $\Delta S$ , in the middle row of Fig. 5. As strain increases, the structure factor difference shows the intensity increasing along the velocity axis, which is represented by the butterfly pattern. The butterfly pattern has been observed in many experimental works by scattering [8,11,13]. Considering that the structure factor analyzes the microstructure in the reciprocal space, which has an inverse relationship with the real space, the butterfly pattern indicates a

preferential alignment of particles along the vorticity direction.

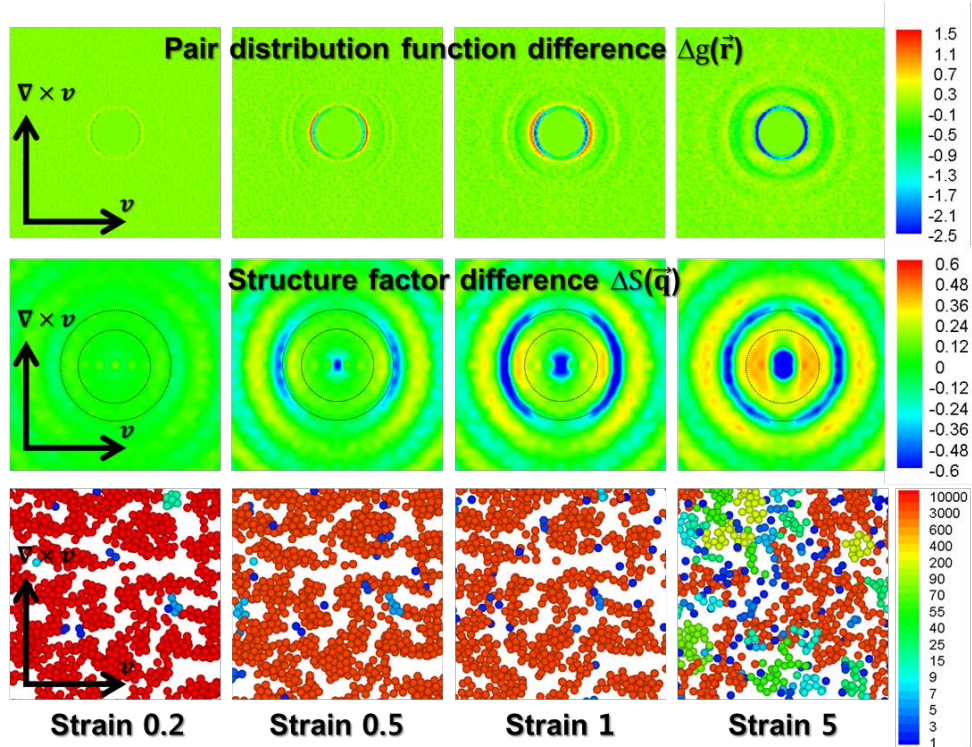


**Fig. 8.** Pair distribution function difference ( $\Delta g(\mathbf{r}, \gamma) = g(\mathbf{r}, \gamma) - g(\mathbf{r}, 0)$ ) (top row) and structure factor difference ( $\Delta S(\mathbf{q}, \gamma) = S(\mathbf{q}, \gamma) - S(\mathbf{q}, 0)$ ) (middle row) in the velocity ( $\mathbf{v}$ )–vorticity ( $\nabla \times \mathbf{v}$ ) plane. Snapshots of the particle configuration (bottom row). The images show the particles in the velocity ( $\mathbf{v}$ )–vorticity ( $\nabla \times \mathbf{v}$ ) plane sliced with a thickness of  $4a$ . The color indicates the size of the cluster to which the particles belong. The black circles in the structure factor difference indicate the regime corresponding to the nearest neighbor structure.

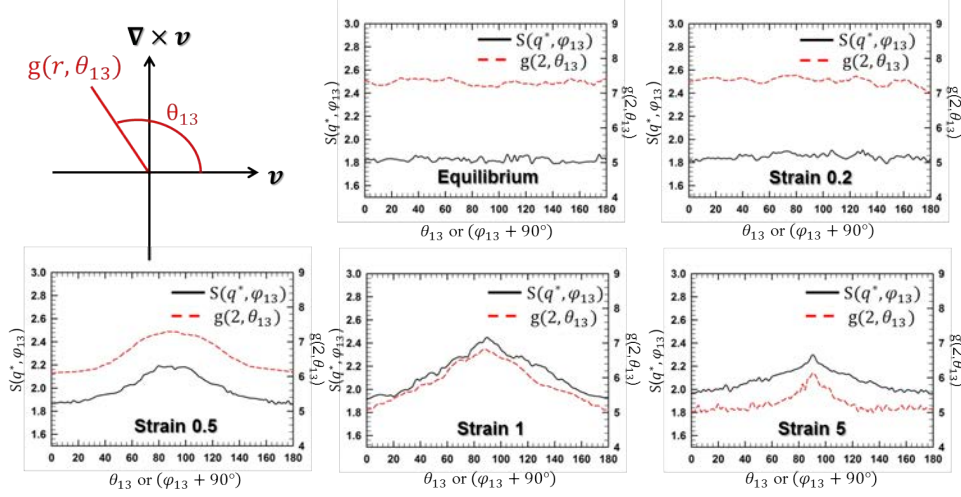


**Fig. 9.** Angular variation of pair distribution function  $g(2, \theta_{13})$  and structure factor  $S(q^*, \varphi_{13} + 90)$  in velocity ( $\mathbf{v}$ )-vorticity ( $\nabla \times \mathbf{v}$ ) plane.

Particle alignment along the vorticity axis has been observed in experiments on near-hard sphere colloidal suspensions as well [24]. In case of hard sphere colloidal suspensions, the structural anisotropy along the vorticity has been considered to be induced by the hydrodynamic interactions between particles [29]. However, in our study, the structural anisotropy along the vorticity direction cannot be credited to the hydrodynamic interaction, because the hydrodynamic interaction between particles is ignored. The quantitative analysis through the angular variation of the pair distribution function  $g(2, \theta_{13})$  and the structure factor  $S(q^*, \varphi_{13} + 90)$  in Fig. 9 suggests an explanation. At equilibrium state of strain 0, as in the velocity ( $\mathbf{v}$ )-gradient ( $\nabla \mathbf{v}$ ) plane, both the pair distribution function and the structure factor are isotropic, which is represented by flat curves. At strain 0.2, the pair distribution function and the structure factor are still largely isotropic. Initially, the imposed shear flow induces no structural anisotropy along the vorticity direction. However, as strain increases further, the colloidal gel shows structural anisotropy along the vorticity axis. At strain 0.5, near the velocity axis ( $\theta_{13} = \varphi_{13} + 90 = 0$  or  $180$ ), the pair distribution function and structure factor decrease. Whereas, near the vorticity axis ( $\theta_{13} = \varphi_{13} + 90 = 90$ ), the pair distribution function maintains its initial value at strain 0 and some increase in structure factor is observed. As shear flow can be considered as a linear combination of rotation field and extension field, [51] the convection of the flow competes with the attractive inter-particle force to induce structural rupture in the direction of the velocity ( $\mathbf{v}$ ) axis. In contrast, lacking any vorticity direction component in the shear flow, only an

attractive interparticle force acts on the network structure along the vorticity direction. Thus, the network structure in the vorticity direction undergoes relatively less microstructural change and maintains structure with increasing shear strain as opposed to the structure along the velocity direction. The net effect is a comparatively higher value of the pair distribution function and the structure factor along the vorticity axis as compared to the velocity direction.

As strain increases more, at strain 1, the structural anisotropy along the vorticity axis intensifies. Near the vorticity axis, where the colloidal gel has a low probability of rupture, the colloidal gel maintains its structure and only slight decrease in the pair distribution function is observed. On the other hand, near the velocity axis, where the colloidal gel has a high probability of rupture, rapid decrease in the pair distribution function is observed. As the strain increases further, however, the shearing disrupts the overall gel structure, even in the vorticity axis direction. Therefore, at strain 5, the pair distribution function decreases in all directions including the vorticity axis. However, the colloidal gel still shows preferred structural anisotropy along the vorticity axis, even though it is weakened.

The anisotropic structure in the velocity ( $\mathbf{v}$ )- vorticity ( $\nabla \times \mathbf{v}$ ) plane can be related to a linear combination of spherical harmonic terms,  $2X_0^{(2)} - X_1^{(2)}$ , which is shown in the inset of Fig. 10(A). In the Fig. 10(A), a linear combination of spherical harmonic coefficients,  $2g_0^{(2)} - g_1^{(2)}$ , which is related to the intensity of  $2X_0^{(2)} - X_1^{(2)}$ , is exhibited. Initially, at strain 0,  $2g_0^{(2)} - g_1^{(2)}$  shows flat curve consistent with an isotropic structure. As strain increases, two peaks are observed at  $r \cong 1.95$  and in between 2 and 2.15. At  $r \cong 1.95$ , the peak shows minima of negative value and in between 2 and 2.15, the peak shows maxima with positive value. Considering that  $2X_0^{(2)} - X_1^{(2)}$  describes anisotropic structure aligned preferentially along the vorticity axis, as shown in the inset of the Fig. 10 (A), the positive and negative value of  $2g_0^{(2)} - g_1^{(2)}$  indicate the anisotropic structure along the vorticity axis and velocity axis, respectively. Therefore, the small negative peaks at  $r \cong 1.95$  can be interpreted as a weak structural anisotropy in the velocity direction. On the other hand, the large positive peaks in in between 2 and 2.15 can be associated with the anisotropic structure along the vorticity direction.

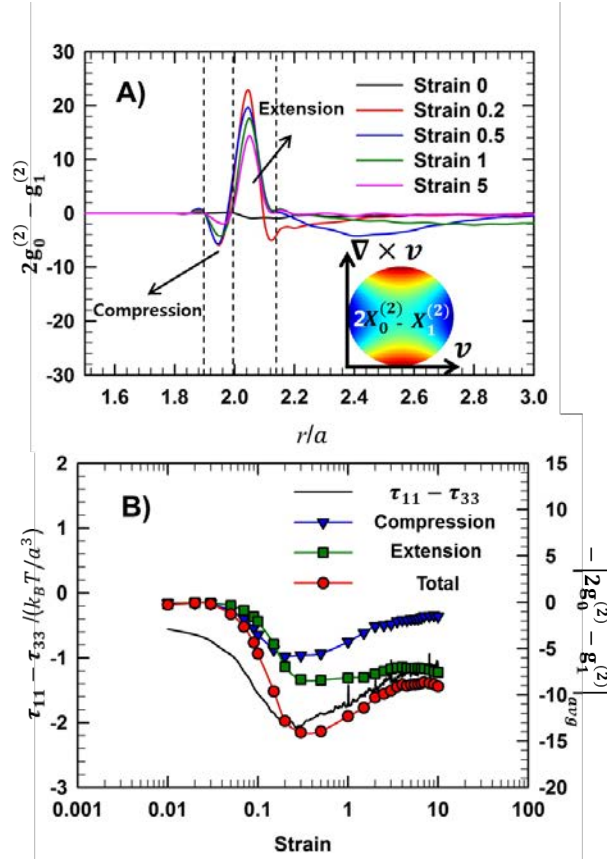


**Fig. 10.** **A)** A combination of spherical harmonic functions  $2X_0^{(2)} - X_1^{(2)}$  (Inset) and coefficients  $2g_0^{(2)} - g_1^{(2)}$ , which correspond to the structural anisotropy along vorticity direction in the velocity ( $\mathbf{v}$ ) - vorticity ( $\nabla \times \mathbf{v}$ ) plane. Dotted lines denote the compression part and the extension part. **B)** Absolute value of  $2g_0^{(2)} - g_1^{(2)}$  averaged over compressional part (blue down triangle) and extensional part (green square) and sum (red circle) as a function of strain ( $\gamma$ ). Black solid line displays normal stress difference  $\tau_{11} - \tau_{33}$  (N1+N2).

As in the velocity ( $\mathbf{v}$ )-gradient ( $\nabla \mathbf{v}$ ) plane, where the structural anisotropy exhibits a strong correlation to the shear stress  $\tau_{12}$ , the structural anisotropy in the velocity ( $\mathbf{v}$ )-vorticity ( $\nabla \times \mathbf{v}$ ) plane is also closely correlated to the rheological response defined by the difference between the normal stresses  $\tau_{11}$  and  $\tau_{33}$ . The relationship between  $2g_0^{(2)} - g_1^{(2)}$ , which describes the degree of the structural anisotropy in the velocity ( $\mathbf{v}$ )-vorticity ( $\nabla \times \mathbf{v}$ ) plane, and the normal stress

difference,  $\tau_{11} - \tau_{33}$ , is given as: [36]

$$\tau_{11} - \tau_{33} = \frac{2}{15} \pi \rho^2 \int_0^\infty r^3 \left( 2g_0^{(2)} - g_1^{(2)} \right) \left( \frac{d\phi}{dr} \right) dr \quad (23)$$

As mentioned in the previous part, because of the bond length dependent inter-particle potential, the above equation is not automatically applicable to our work. Therefore, we compared  $2g_0^{(2)} - g_1^{(2)}$  to  $\tau_{11} - \tau_{33}$  to assess this relationship. To compare  $2g_0^{(2)} - g_1^{(2)}$  to  $\tau_{11} - \tau_{33}$ ,  $2g_0^{(2)} - g_1^{(2)}$  was averaged in compressional part and extensional part, which are denoted by dotted lines in Fig. 10 (A). Because both of compressional part (negative  $2g_0^{(2)} - g_1^{(2)}$  and positive  $\left(\frac{d\phi}{dr}\right)$  due to repulsive force by surface potential) and extensional part (positive  $2g_0^{(2)} - g_1^{(2)}$  and negative  $\left(\frac{d\phi}{dr}\right)$  due to attractive force by bonding potential) contribute negatively to  $\tau_{11} - \tau_{33}$ , we compared the sum of  $-\left|2g_0^{(2)} - g_1^{(2)}\right|_{avg}$  in the compression part and extension part to  $\tau_{11} - \tau_{33}$ . Figure. 10 (B) shows the evolution of  $-\left|2g_0^{(2)} - g_1^{(2)}\right|_{avg}$  and  $\tau_{11} - \tau_{33}$  as a function of strain ( $\gamma$ ).  $-\left|2g_0^{(2)} - g_1^{(2)}\right|_{avg}$  in the compression part, where  $2g_0^{(2)} - g_1^{(2)}$  describes the structure along the velocity axis, shows undershoot behavior. The undershoot of  $-\left|2g_0^{(2)} - g_1^{(2)}\right|_{avg}$  in the compression part can be understood as the structural rupture along the velocity axis. On the other hand,  $-\left|2g_0^{(2)} - g_1^{(2)}\right|_{avg}$  in the extension part does not exhibit clear undershoot behavior. Given that the  $2g_0^{(2)} - g_1^{(2)}$  in the extension part describes the structure along the vorticity direction, the lack of an undershoot behavior can be understood as a result of a constant structure along the vorticity axis. The undershoot evident in the sum of  $-\left|2g_0^{(2)} - g_1^{(2)}\right|_{avg}$  qualitatively corresponds to the undershoot of the normal stress difference  $\tau_{11} - \tau_{33}$ , signifying strong correlation between structural anisotropy and the rheological response.

### 3) Gradient-vorticity ( $\nabla\mathbf{v} - \nabla \times \mathbf{v}$ ) plane

The pair distribution function difference,  $\Delta g$ , structure factor difference  $\Delta S$ , and particle configuration of the colloidal gel in the gradient ( $\nabla\mathbf{v}$ )–vorticity ( $\nabla \times \mathbf{v}$ ) plane are shown in Fig. 11.

The result in the gradient( $\nabla\mathbf{v}$ )-vorticity( $\nabla\times\mathbf{v}$ ) plane has much in common with the result in the velocity( $\mathbf{v}$ )-vorticity( $\nabla\times\mathbf{v}$ ) plane. As strain increases, the innermost ring of the pair distribution function difference in the top row shows a decrease along the gradient direction. Whereas, in the vorticity direction, the innermost ring exhibits a comparatively slight decrease in the pair distribution function. The partial structural change, which results in structural anisotropy along the vorticity axis, is demonstrated in the structure factor difference as well. In the middle row of Fig. 11, as strain increases, the structure factor difference displays an increase in intensity along the gradient axis, which is described by butterfly pattern. The butterfly pattern is similar to that of the velocity( $\mathbf{v}$ ) - vorticity( $\nabla\times\mathbf{v}$ ) plane and can again be interpreted as the structural anisotropy with preference along the vorticity axis.

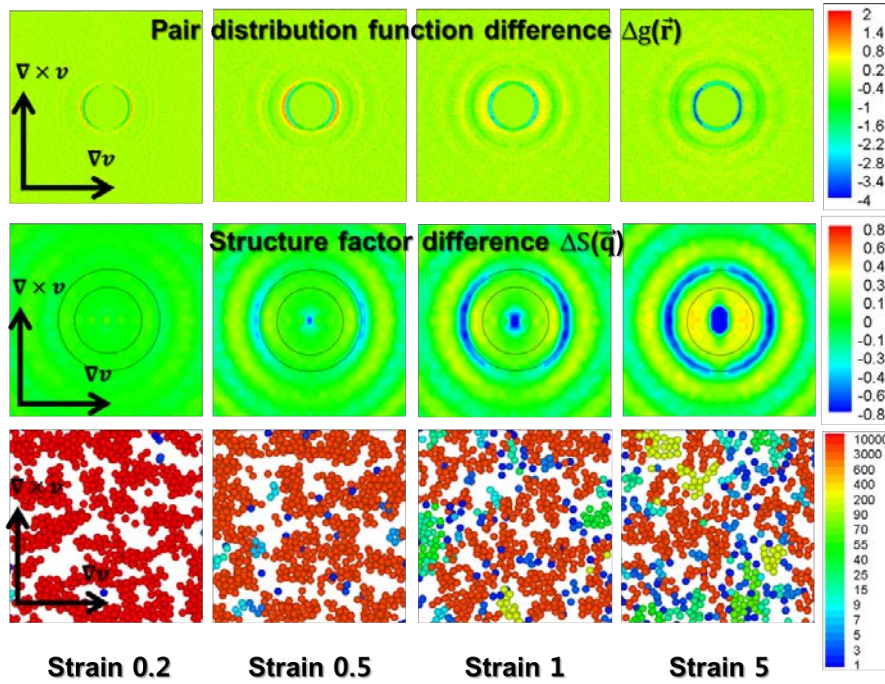


**Fig. 11.** Pair distribution function difference ( $\Delta g(\mathbf{r}, \gamma) = g(\mathbf{r}, \gamma) - g(\mathbf{r}, 0)$ ) (top row) and structure factor difference ( $\Delta S(\mathbf{q}, \gamma) = S(\mathbf{q}, \gamma) - S(\mathbf{q}, 0)$ ) (middle row) in gradient( $\nabla\mathbf{v}$ )-vorticity( $\nabla\times\mathbf{v}$ ) plane. Snapshots of the particle configuration. (bottom row) The images show the particles in the velocity-gradient plane sliced with a thickness of  $4a$ . The color indicates the size of the cluster to which the particles belong. The black circles in the structure factor difference indicate the regime corresponding to the nearest neighbor structure.

Figure. 12 shows the angular variation of the pair distribution function  $g(2, \theta_{23})$  and the structure factor,  $S(q^*, \varphi_{23} + 90)$ . At equilibrium state of strain 0, the pair distribution function and the structure factor show flat curves, which indicates a relatively isotropic structure. At strain 0.2, the pair distribution function and the structure factor do not show any remarkable changes. As strain increases further, a decrease in the pair distribution function is observed near the gradient axis ( $\theta_{23} = \varphi_{23} + 90 = 0$  or  $180$ ). On the other hand, near the vorticity axis ( $\theta_{23} = \varphi_{23} + 90 = 90$ ), the pair distribution function undergoes a comparatively small decrease and shows a maximum value, which indicates the structural anisotropy along the vorticity axis. In addition, the structure factor shows a similar change, which shows the maximum value near the vorticity axis. This evolution of the structural anisotropy along the vorticity axis in the gradient ( $\nabla \mathbf{v}$ )–vorticity ( $\nabla \times \mathbf{v}$ ) plane is similar to that of the velocity ( $\mathbf{v}$ )–vorticity ( $\nabla \times \mathbf{v}$ ) plane. Because the shear flow has a component in the gradient direction, the colloidal gel experiences structural rupture in the gradient direction. However, due to the absence of vorticity direction component in shear flow, the shear flow has comparatively less effect on the structure in the vorticity direction. Again, the attractive particle interaction dominates the structure along the vorticity direction, leading to the butterfly-like patterns.

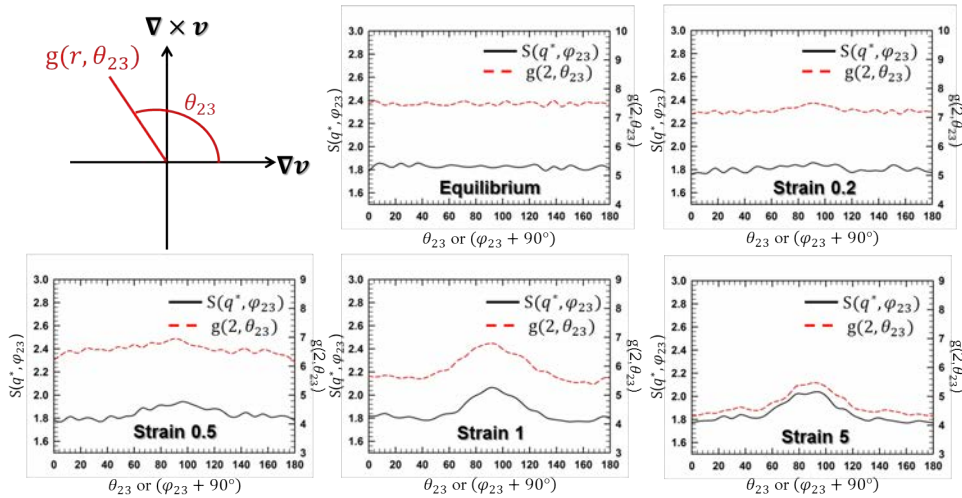


**Fig. 12.** Angular variation of pair distribution function ( $g(2, \theta_{23})$ ) and structure factor  $S(q^*, \varphi_{23} + 90)$  in the gradient ( $\nabla \mathbf{v}$ )–vorticity ( $\nabla \times \mathbf{v}$ ) plane.

The anisotropic structure in the gradient ( $\nabla \mathbf{v}$ )–vorticity ( $\nabla \times \mathbf{v}$ ) plane can be described by the linear combination of spherical harmonic terms,  $2X_0^{(2)} + X_1^{(2)}$ , which is shown in the inset of Fig. 13(A). In Fig. 13(A),  $2g_0^{(2)} + g_1^{(2)}$ , which denotes the intensity of  $2X_0^{(2)} + X_1^{(2)}$ , is shown as a

function of distance,  $r$ . At strain 0,  $2g_0^{(2)} + g_1^{(2)}$  exhibits a flat curve, due to the isotropic structure at equilibrium state. As strain increases, at  $r \cong 2$  and in between 2 and 2.15, two peaks are observed. At  $r \cong 2$ , the peak shows negative minima, which describes the structure along the gradient axis. As strain increased, the peak around  $r \cong 2$  gradually disappears. This disappearance indicates that the structure along the gradient direction is ruptured. In between 2 and 2.15, the peak shows positive maxima, which demonstrates the structure along the vorticity direction. In contrast to the peak at  $r \cong 2$ , which exhibits gradual decrease due to the structure rupture along the gradient axis, the peak between 2 and 2.15 maintains its value except for a small, initial decrease. This signifies that the structure along the vorticity direction experiences less microstructural change.

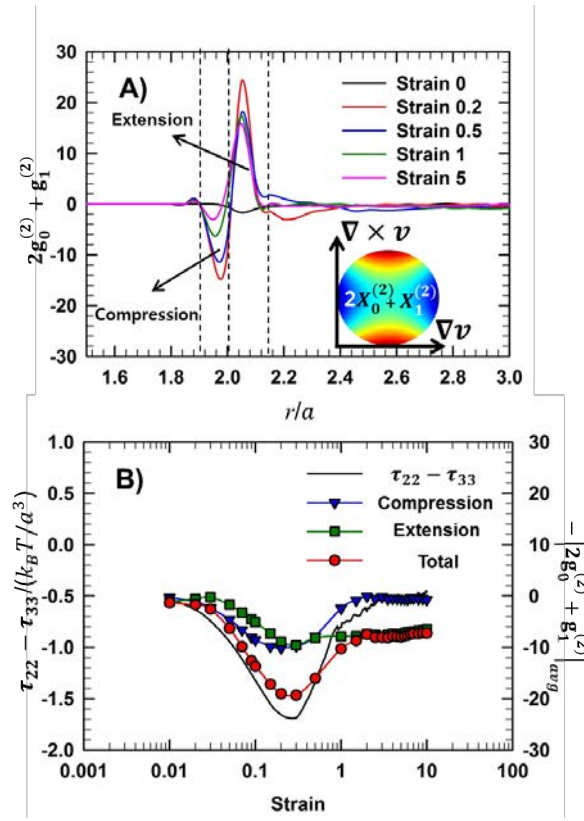


**Fig. 13. A)** A combination of spherical harmonic functions  $2X_0^{(2)} + X_1^{(2)}$  (Inset) and coefficients  $2g_0^{(2)} + g_1^{(2)}$ , which correspond to the structural anisotropy along vorticity direction in gradient ( $\nabla\mathbf{v}$ )–vorticity ( $\nabla\times\mathbf{v}$ ) plane. Dotted lines denote the compression part and the extension part. **B)** Absolute value of  $2g_0^{(2)} + g_1^{(2)}$  averaged over compressional part (blue down triangle) and extensional part (green square) and sum (red circle) as a function of strain ( $\gamma$ ). Black solid line displays normal stress difference,  $\tau_{22} - \tau_{33}$  (N2).

The analysis of the spherical harmonic expansion of the pair distribution function signifies that the structural anisotropy in the gradient( $\nabla\mathbf{v}$ )-vorticity( $\nabla\times\mathbf{v}$ ) plane is closely linked to the second normal stress difference,  $\tau_{22} - \tau_{33}$ . Theoretically, the relationship between  $2\mathbf{g}_0^{(2)} + \mathbf{g}_1^{(2)}$  and  $\tau_{22} - \tau_{33}$  is given as follows [36]:

$$\tau_{22} - \tau_{33} = \frac{2}{15} \pi \rho^2 \int_0^\infty r^3 \left( 2\mathbf{g}_0^{(2)} + \mathbf{g}_1^{(2)} \right) \left( \frac{d\phi}{dr} \right) dr \quad (24)$$

As the above equation is not automatically applicable to our work, we analyzed the correlation between the anisotropic structure and the second normal stress difference by comparing  $2\mathbf{g}_0^{(2)} + \mathbf{g}_1^{(2)}$  to  $\tau_{22} - \tau_{33}$ . To compare  $2\mathbf{g}_0^{(2)} + \mathbf{g}_1^{(2)}$  to  $\tau_{22} - \tau_{33}$ ,  $2\mathbf{g}_0^{(2)} + \mathbf{g}_1^{(2)}$  was averaged in compressional part and extensional part, individually. Because both of the compression part (negative  $2\mathbf{g}_0^{(2)} + \mathbf{g}_1^{(2)}$  and positive  $\left(\frac{d\phi}{dr}\right)$  due to repulsive force by surface potential) and the extension part (positive  $2\mathbf{g}_0^{(2)} + \mathbf{g}_1^{(2)}$  and negative  $\left(\frac{d\phi}{dr}\right)$  due to attractive force by bonding potential) contribute negatively to  $\tau_{22} - \tau_{33}$ , we compared the sum of  $-\left|2\mathbf{g}_0^{(2)} + \mathbf{g}_1^{(2)}\right|_{avg}$  in the compression part and the extension part to  $\tau_{22} - \tau_{33}$ . Figure. 13 (B) shows the evolution of  $-\left|2\mathbf{g}_0^{(2)} + \mathbf{g}_1^{(2)}\right|_{avg}$  and  $\tau_{22} - \tau_{33}$  as a function of strain. In the case of compression part, where negative  $2\mathbf{g}_0^{(2)} + \mathbf{g}_1^{(2)}$  describes the anisotropic structure along the gradient axis,  $-\left|2\mathbf{g}_0^{(2)} + \mathbf{g}_1^{(2)}\right|_{avg}$  shows an undershoot that can be attributed to the structural rupture along the gradient axis. On the other hand, in the extension part, where positive  $2\mathbf{g}_0^{(2)} + \mathbf{g}_1^{(2)}$  is related to the anisotropic structure along the vorticity axis,  $-\left|2\mathbf{g}_0^{(2)} + \mathbf{g}_1^{(2)}\right|_{avg}$  shows little undershoot. As in the velocity( $\mathbf{v}$ )-vorticity( $\nabla\times\mathbf{v}$ ) plane, the absence of undershoot can be correlated to the maintenance of the structure along the vorticity axis. The sum of  $-\left|2\mathbf{g}_0^{(2)} + \mathbf{g}_1^{(2)}\right|_{avg}$  in the compression part and the extension part demonstrates undershoot behavior, which corresponds to the undershoot of  $\tau_{22} - \tau_{33}$ .

### C. Overshoot of alignment factor $A_f$ and modified stress-SANS rule

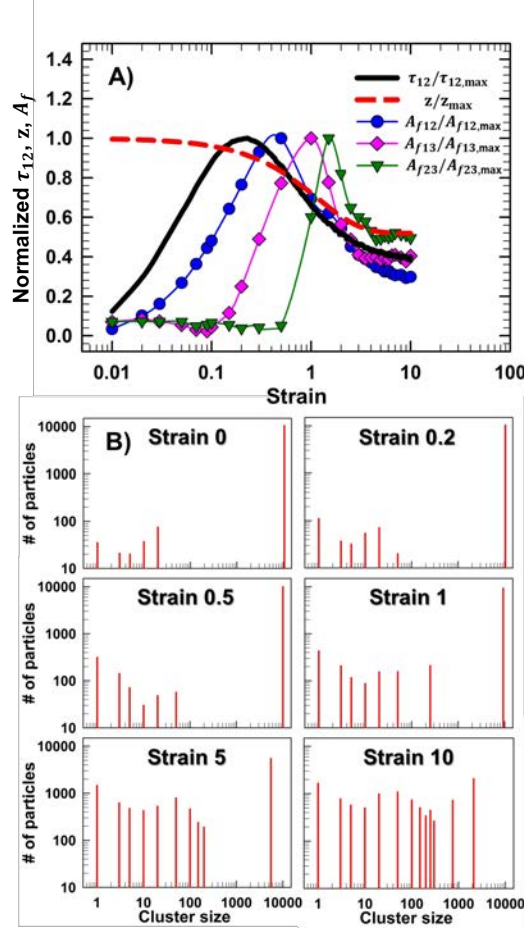


**Fig. 14. A)** Normalized shear stress ( $\tau_{12}/\tau_{12,max}$  (black solid line)), average bond number ( $z/z_{max}$  (red dashed line)), and alignment factors ( $A_{f12}/A_{f12,max}$  (blue circle),  $A_{f13}/A_{f13,max}$  (pink diamond),  $A_{f23}/A_{f23,max}$  (green triangle)) at Pe 200. **B)** Particle number distribution according to the cluster size at each strain at Pe 200.

So far, the shear-induced anisotropic structure of the colloidal gel has been quantitatively analyzed through the pair distribution function and the structure factor. The analysis through the pair distribution function is intuitive and easily understandable. In particular, the spherical harmonic expansion of the pair distribution function shows a close connection between the structural anisotropy and rheological behavior. However, a simplified analysis of shear-induced structural anisotropy is often performed in experiments. In experimental studies, the structural anisotropy is usually quantified through an order parameter that is a weighted average of the scattering pattern, which corresponds to the structure factor in this study. In this section, the alignment factor will be further analyzed and correlated to the stress response, which is expected to provide especially useful

information for comparison to experiments.

A scalar order parameter of the structural anisotropy can be quantified using the alignment factor ( $A_f$ ) given as the Eq. 20. Figure. 14(A) shows normalized shear stress ( $\tau_{12}/\tau_{12,\max}$ ), alignment factor ( $A_f/A_{f,\max}$ ), and average bond number ( $z/z_{\max}$ ) under startup of shear at Pe 200. The alignment factors in all three planes show overshoot behavior that is similar to the shear stress. In the velocity ( $\mathbf{v}$ )-gradient ( $\nabla\mathbf{v}$ ) plane, where the structural anisotropy in the compressional axis direction is observed, the alignment factor  $A_{f12}$  increases as soon as the shear flow is applied. However, in the velocity ( $\mathbf{v}$ )-vorticity ( $\nabla\times\mathbf{v}$ ) plane and the gradient ( $\nabla\mathbf{v}$ )-vorticity ( $\nabla\times\mathbf{v}$ ) plane where the colloidal gel shows the structural anisotropy along the vorticity direction, the alignment factor does not increase instantly and displays a delayed response. This can be attributed to the difference in the mechanism inducing structural anisotropy. In the velocity ( $\mathbf{v}$ )-gradient ( $\nabla\mathbf{v}$ ) plane, the structural anisotropy can be caused not only by the structural breakup that depletes the particles along the extensional axis but also by the structural deformation that convects the particles together along the compressional axis. Therefore, the initial strain increase without significant bond breaking leads to an increase in  $A_{f12}$ . Indeed, as shown in Fig. 14(A), while the average bond number does not show any remarkable change in the beginning of shear startup, the alignment factor in the velocity-gradient plane  $A_{f12}$  demonstrates a clear increase. In contrast, according to the angular variation of the pair distribution function and the structure factor, it has been shown that the structural anisotropy along the vorticity axis is induced by structural rupture, which prefers the velocity and gradient direction. Thus, the initial structural deformation without bond breaking does not increase the alignment factor in the velocity-vorticity plane and the gradient-vorticity plane. As shown in the Fig. 14(A), the delayed increase in alignment factors  $A_{f13}$  and  $A_{f23}$  accompanies a rupture of colloidal gel structure, which is represented by the decrease in the average bond number.

As strain increases further, the colloidal gel shows a decrease in the alignment factors in all three planes. The decrease in the alignment factor is linked to the structural change from the percolated network to small gel fragments. Fig. 14(B) shows the particle number distributions according to the cluster size. Here, abscissa represents the size of the cluster, to which the particles belong, and ordinate indicates the number of the particles belonging to each cluster size, which is the product of cluster size and the number of clusters. At strain 0, the particle number distribution shows a significant peak around 10,000, which describes the percolated network chain. Under the startup shear flow, the peak is maintained until strain 1 and this indicates that the colloidal gel maintains the

network structure. However, at higher strain, this peak shrinks and moves to smaller sizes. In addition, there appears several peaks in the cluster size of dozens to hundreds. This indicates a structural change from percolated network to several clusters and flocs. As the anisotropic gel structure turns into smaller, isotropic fragments, the alignment factors in the velocity ( $\mathbf{v}$ )-vorticity ( $\nabla \times \mathbf{v}$ ) plane and the gradient ( $\nabla \mathbf{v}$ )-vorticity ( $\nabla \times \mathbf{v}$ ) plane decrease. This result corresponds with the change of the angular variation of the pair distribution function and the structure factor, which shows the decrease in the structural anisotropy with the overall decrease of the pair distribution function and the structure factor. The colloidal gel shows similar overshoot behavior in the alignment factor at various Pe values (Alignment factor changes and principal axis angle changes at various Pe values are given in Appendix A).

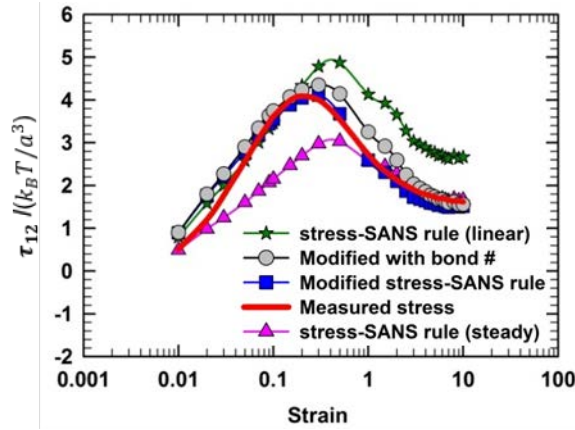


**Fig. 15.** Measured and predicted stress responses of the colloidal gel at Pe 200. Stress responses are predicted using stress-SANS rule and modified stress-SANS rule. “stress-SANS (Linear)” indicates the use of the stress SANS coefficients defined on the basis of linear rheological behaviors. In the case of “stress-SANS (steady)”, steady shear measurements are used to define the stress SANS coefficients. “Modification (bond number)” signifies the modified stress-SANS rule in which structure parameter

( $\lambda$ ) is replaced with normalized average bond number  $\left( \frac{z(\gamma)}{z_{init}} \right)$ .

The overshoot of the alignment factor can be linked to the stress response by the stress-SANS rule: [26]

$$\sigma = G_0 \left[ C(\gamma) A_{f12} \right]^{1/2} \sin(2\varphi_{12,0}). \quad (25)$$

Here,  $G_0$  and  $C(\gamma)$  are shear modulus and the stress-SANS coefficient which is defined from steady shear measurement. The stress-SANS rule has been applied to systems such as micellar

solution [25,52], which is assumed to have the polymeric contribution to rheological behavior. In this work, assuming that the network structure of the colloidal gel also has a similar “polymeric” (elastic springs) contribution to rheological property, we applied the stress-SANS rule to quantitatively associate the structural anisotropy to rheological behavior. Fig. 15, compares the measured shear stress and the shear stress prediction by the stress-SANS rule at  $Pe$  200. (Results for various  $Pe$  values are available in Appendix B). The red solid line denotes the measured stress and pink triangle indicates the stress-SANS calculation with  $C(\gamma)$  defined from the steady shear measurement. Here,  $C(\gamma)$  was determined to a value that minimizes the deviation from the steady measurement using least square method. This manifestation of the stress-SANS rule qualitatively captures the stress response of the colloidal gel, however it underpredicts the stress response at small strain. In addition, the stress overshoot is not properly described. The underprediction at low to moderate strains is a result of using  $C(\gamma)$  derived from the steady shear measurement, where the structure is at its most broken state. One can also define  $C(\gamma)$  from the onset of shear flow using the linear response at low strains. The green stars denote the stress-SANS calculation with  $C(\gamma)$  defined on the basis of the linear rheological behavior. Not surprisingly, as this definition is based on the maximum structured state, this definition overpredicts the stress at higher strain values. This exercise demonstrates that bond breakage and formation must be included in the stress-SANS rule for colloidal gels.

This failure of the naïve stress-SANS rules can be corrected by accounting for the bond number during the startup shear flow. As opposed to the stress-SANS rule, the comparison of stress to structure using the pair distribution function shows a quantitative connection between the structural anisotropy and rheological behavior. This difference arises from the definition of the alignment factor. The pair distribution function and its spherical harmonic expansion involve the information on not only the structural anisotropy, but also size-related structural change, such as breakup of the structure. On the other hand, as it is divided by angular averaged intensity as given in Eq. 20, the alignment factor does not include the information on the size-related structural change. As size-related structural changes play an important role in determining the strength of the material, the naïve stress-SANS rules cannot quantitatively predict nonlinear rheological behaviors, such as stress overshoot, which accompanies rupture of the colloidal gel structure [3,4]. As an alternative, we introduce a method to account for structural rupture through adding the structure kinetics model to the stress-SANS rule and suggest a modified stress-SANS rule. The structure kinetics model is commonly used in theoretical studies to describe the thixotropic materials [53-55]. For example, constitutive equations, which link a stress response to a microstructure, employ a structure kinetics model to include the influence of the

microstructural change [54]. In the structure kinetics model, the instantaneous structure is represented by a dimensionless scalar parameter,  $\lambda$ , which is called structure parameter. The time dependence of  $\lambda$  is described by a differential evolution equation. The evolution equation links the time rate of change of the structure ( $\dot{\lambda}$ ) to the instantaneous flow conditions and structure.

The modified stress-SANS rule can be proposed in the form of:

$$\sigma = S\lambda \left[ \gamma^{1/2} \right] \left[ A_{f12}^{1/2} \sin(2\varphi_{12,0}) \right]. \quad (26)$$

In the Eq. 26, the material constant  $S$  represents the strength of the colloidal gel network structure at equilibrium. The first term on the right-hand side,  $S\lambda$ , corresponds to  $G_0$  in original stress-SANS rule. In the original stress-SANS rule,  $G_0$ , which represents the structural strength, is given as a constant and independent of strain and shear rate. In the modified rule, the effect of structural change on the fraction of the gel network that is connected and contributing to the elastic stress is described by product of a material constant  $S$  and the structure parameter,  $\lambda$ . The structure parameter is given as the solution of the following evolution equation,

$$\frac{d\lambda}{dt} = -k_1 |\gamma| \lambda + k_2 |\gamma|^{0.5} (1 - \lambda). \quad (27)$$

Here, the first term on the right-hand side describes the shear-induced breakup and the second term on the right-hand side expresses shear-induced structure buildup [54]. The analytic solution of the Eq. 27 is given by:

$$\lambda = \left( \frac{k_2 |\gamma|^{0.5}}{k_1 |\gamma| + k_2 |\gamma|^{0.5}} \right) + \left( \frac{k_1 |\gamma|}{k_1 |\gamma| + k_2 |\gamma|^{0.5}} \right) \times \exp \left\{ - \left( k_1 |\gamma| + k_2 |\gamma|^{0.5} \right) \times t \right\} \quad (28)$$

The modified stress-SANS rule introduces three material constants  $S, k_1, k_2$  which need to be determined empirically. In this work, the three constants were determined through fitting the result in Fig. 16. The first row in the Fig. 16 shows the evolutions of the alignment factor  $A_{f12}$  and the principal axis angle  $\varphi_{12,0}$  in the velocity ( $\mathbf{v}$ )-gradient ( $\nabla \mathbf{v}$ ) plane at various Pe values (5, 10, 20, 50, 100, 200). With the evolution results, the best fitting parameters ( $S = 0.025, k_1 = 1.14, k_2 = 15.89$ ), which are optimized to best fit the measured stress for all Pe, were chosen using a polynomial curve fitting technique with least squares method. In the middle of the right hand side of Eq. 26, the

influence of the shear rate, which is described by stress-SANS coefficient  $C(\gamma)$  in the original stress-SANS rule, is represented by  $\gamma^{1/2}$ . Because the shear rate is closely related to the relaxation of the structure, the stress response of the colloidal gel depends on the applied shear rate. In Fig. 3(D), it has been shown that the flow curve of the colloidal gel conforms to the SGR model, which predicts the power law relationship between shear stress and rate with an exponent of 0.5. However, one can expect that at very high shear rates the particles will be fully dispersed and the sample will reach a limiting high shear viscosity plateau. In addition, the stress overshoot in Fig. 3(C) agrees with the SGR model, which demonstrates the stress maximum at a constant strain. Therefore, according to these similarities, the influence of the shear rate on the stress response is represented based on the SGR model, which shows a power law increase of the shear stress with an exponent of 0.5 under start up shear [45]. The last term  $A_{f12}^{1/2} \sin(2\phi_{12,0})$ , which describes the influence of the structural anisotropy, is unchanged from the original stress-SANS rule.

In Fig. 15, blue squares show the stress response calculated by the modified stress-SANS rule. As seen, the modified stress-SANS rule connects the measured metrics of the structure to the stress with quantitative agreement over the entire range of strains probed. Equally successful results are shown for startup flows at other Pe values (Fig. 17 in Appendix B), verifying the hypothesis that the stress-SANS rule must account for direct bonded interactions.

To further explore the theoretical basis of this modified stress-SANS rule, we examine the possible relationship between the structure parameter and the bond network. Theoretically, the structure parameter was originally associated with the number of links between structure elements, such as the bonds between the particles [54,55]. Thus, we replace the structure parameter and its associated kinetic equation with a normalized average bond number,  $\left(\frac{z(\gamma)}{z_{init}}\right)$ . Here,  $z_{init}$  and  $z(\gamma)$  note the average bond number at initial equilibrium state and at strain  $\gamma$ , respectively. The gray circles in the Fig. 15 shows the stress responses calculated from the stress-SANS rule with this replacement using the average bond number directly calculated during the simulation. The stress-SANS rule modified with the average bond number nearly quantitatively predicts stress response, which validates the underlying hypothesis of the modified stress-SANS rule with the structure kinetics model. Again, as shown in the Appendix B, this result holds for startup flows at other Pe values. This result verifies the correlation between the structure parameter and the degree of bond formation in colloidal gels. Interestingly, it suggests that the modified stress-SANS rule can be interpreted to study bond rupture in colloidal gels.

#### IV. Conclusions

A modified Brownian Dynamics simulation that explicitly accounts for surface bond formation is used to study the shear-induced structural anisotropy during flow startup for colloidal gels with the goals of demonstrating the quantitative connection between the real space microstructure, scattering patterns, and measured deviatoric stress tensor. Under startup shear flow, the colloidal gel shows structural anisotropy predominantly along the direction of the compressional axis, with bond rupture along the extensional axis, in qualitative agreement with experiments. This also results in an anisotropy aligned along the vorticity axis, again in agreement with recent experimental results. The structural anisotropy in the direction of the compressional axis arises from initial structural deformation, which condenses the particles along the compressional axis, and the rupture of the colloidal gel structure, which is preferred in the extensional axis direction. The structural anisotropy along the vorticity axis direction is attributed to the same shear-induced structural rupture when viewed in the appropriate projection. Because the shear flow acts in the velocity-gradient plane of flow, it competes with the attractive interparticle force to break the structure along the velocity direction and the gradient direction. On the other hand, with no vorticity direction component in the shear flow, the attractive inter-particle force maintains the network structure and the colloidal gel undergoes relatively less microstructural change in the vorticity direction. The structural changes in the velocity -gradient plane leads to an anisotropic structure orientation in the direction of the vorticity axis evident in the velocity-vorticity and gradient-vorticity planes of observation. The evolution of structural anisotropy with strain was quantitatively linked to nonlinear stress response that exhibits a strong stress overshoot through a spherical harmonic expansion of the pair distribution function and a stress-SANS rule. Consistent with micromechanical theory, the spherical harmonic expansion of the pair distribution function showed a quantitative correlation between the structural anisotropy and the macroscopic stress response. Importantly, we demonstrate that a modified stress-SANS rule that explicitly includes bond formation and rupture via a structure kinetics model can quantitatively relate the nonlinear stress evolution upon flow startup to the order parameters. Finally, analysis of the bond network in the simulations proves the proposed hypothesis that the structure parameter is associated with the number of bonds between particle surfaces. This work provides a quantitative connection between the evolution of the deviatoric stresses in the flow startup of a colloidal gel and the microstructure, as can be determined by direct microscopy and scattering, as well as a method to connect this back to the bond network. As such, it is useful for both designing and interpreting measurements of colloidal gel rheology, as well as in designing better quantitative theories for predicting colloidal gel rheology. We caution, however, that our work neglects hydrodynamic

interactions, which are known to play an important role in both gel formation and gel rheology. Thus, comparisons with experiment should keep this approximation in mind.

### **Acknowledgment**

The authors are grateful to Simon Rogers (UIUC) for valuable discussions. Norman J. Wagner acknowledges support of the National Science Foundation grant number CBET 312146. This work was supported by the National Research Foundation of KOREA (NRF) grant (No. 2013R1A2A2A07067387) funded by the Korea government.

**Appendix A: Alignment factor change and principal axis angle change**

Figure. 16 shows alignment factor change and principal axis angle change in three orthogonal planes of velocity-gradient, velocity-vorticity, and gradient-vorticity for various Pe values (5, 10, 20, 50, 100, 200). Results were calculated and averaged for five different simulation sets with different random motion and initial configuration of the particles.

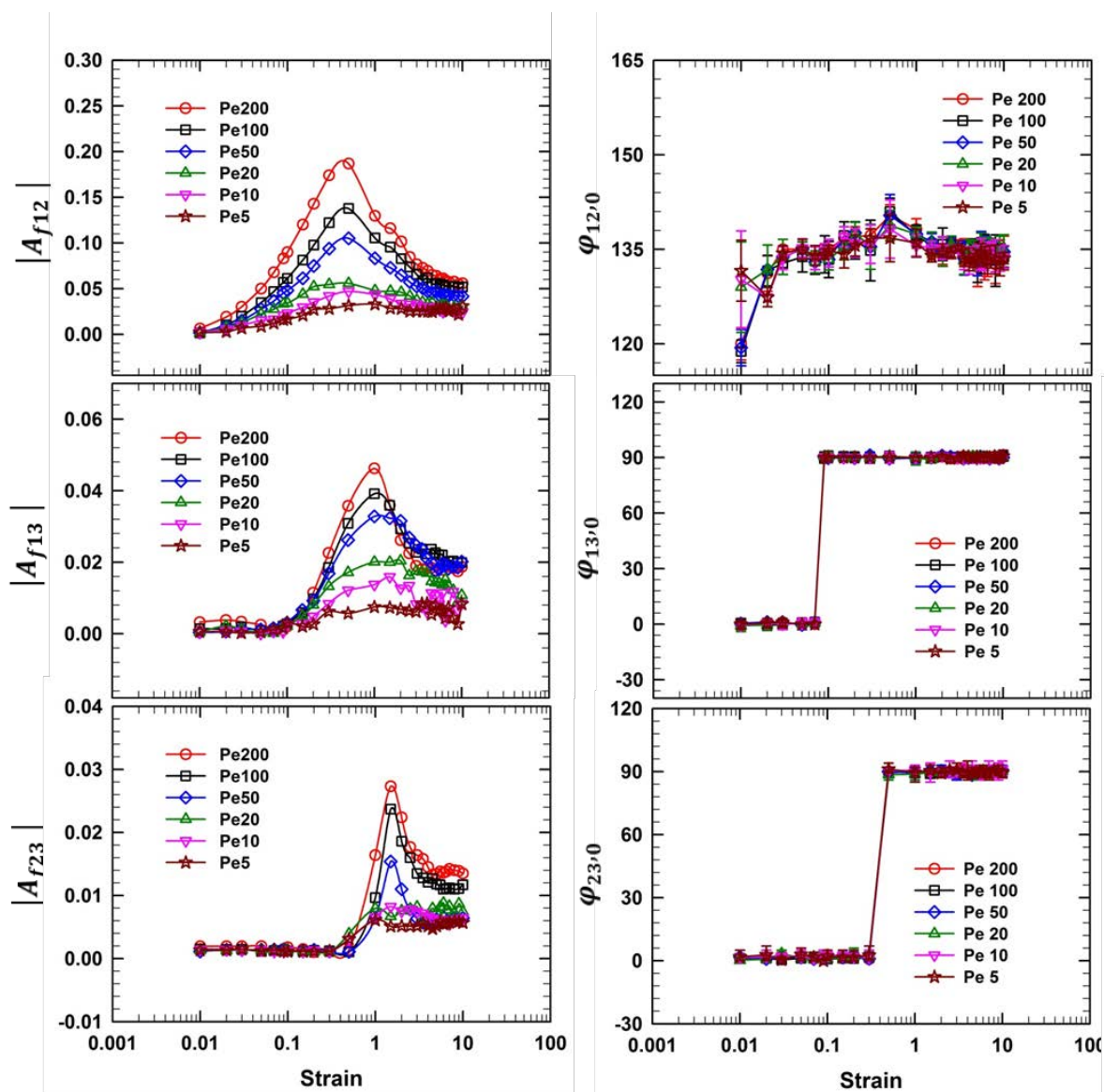


**Fig. 16.** Alignment factor ( $A_{f12}, A_{f13}, A_{f23}$ ) change and principal axis angle ( $\varphi_{12,0}, \varphi_{13,0}, \varphi_{23,0}$ ) change in velocity ( $\mathbf{v}$ )-gradient ( $\nabla\mathbf{v}$ ) plane, velocity ( $\mathbf{v}$ )-vorticity ( $\nabla\times\mathbf{v}$ ) plane, and gradient ( $\nabla\mathbf{v}$ )-vorticity ( $\nabla\times\mathbf{v}$ ) plane. Results are shown for various Pe values as indicated.

## Appendix B : Measured and predicted stress response

In Fig. 17, stress response predictions for different Pe values (5, 10, 20, 50, 100, 200) are shown. Stress responses are calculated from stress-SANS rule and modified stress-SANS rule with the alignment factor change results in Fig. 16. Results were compared with measured stress response (Red Solid line).

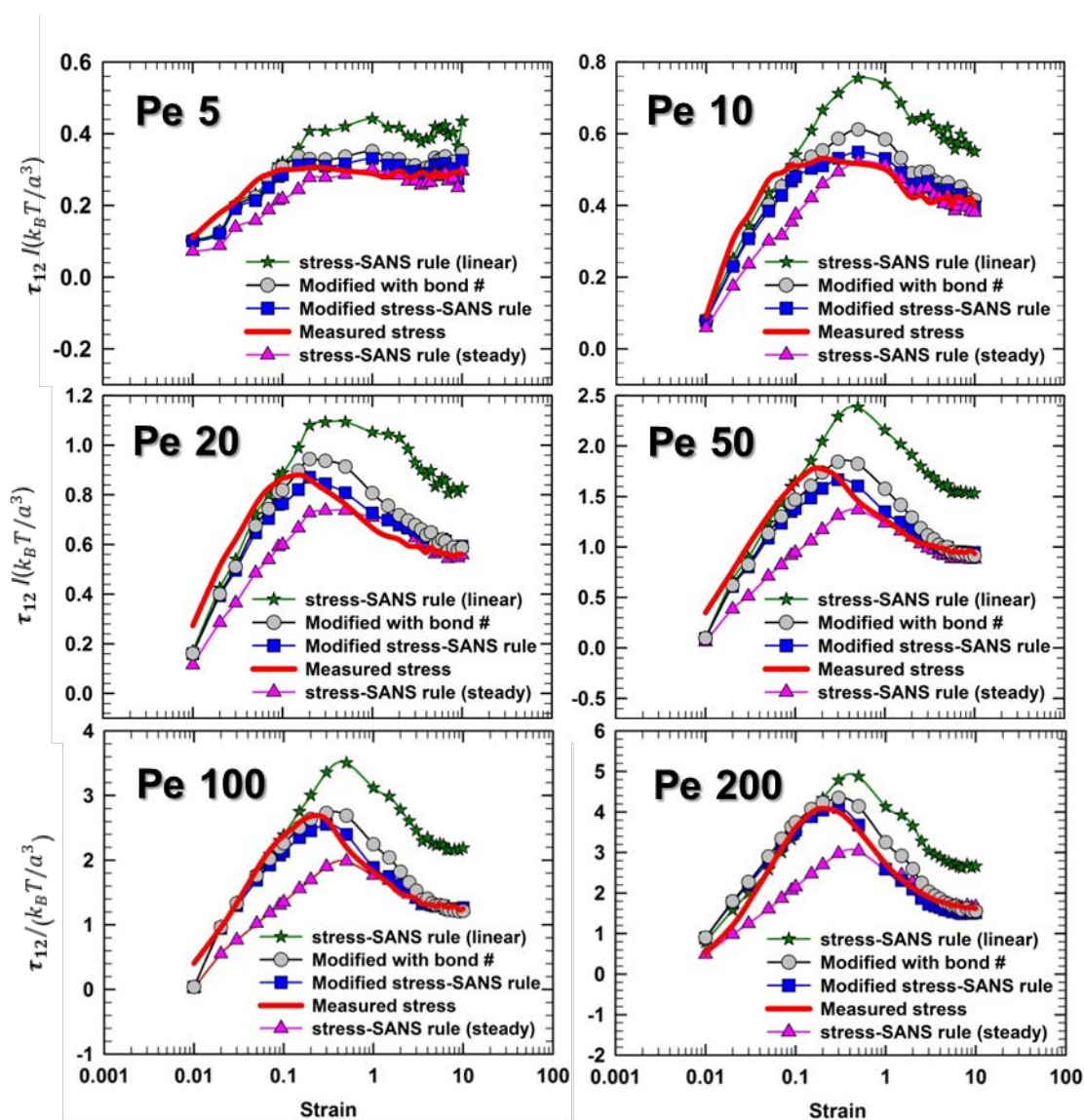


**Fig. 17.** Measured and predicted stress responses of the colloidal gel at various Pe values. Stress responses are predicted using Stress SANS rule and modified Stress SANS rule. Stress-SANS (Linear) indicates the use of the stress SANS coefficients defined on the basis of linear rheological behaviors. In the case of stress-SANS (steady), steady shear measurements are used to define the stress SANS coefficients. Modification (bond number) signifies the modified stress-SANS rule in which structure

parameter  $(\lambda)$  is replaced with normalized average bond number  $\left(\frac{z(\gamma)}{z_{init}}\right)$ .

## References

- [1] Lu, P. J., E. Zaccarelli, F. Ciulla, A. B. Schofield, F. Sciortino, and D. A. Weitz, “Gelation of particles with short-range attraction,” *Nature* **453**, 499–504 (2008).
- [2] Zaccarelli, E., “Colloidal gels: equilibrium and non-equilibrium routes,” *J. Phys.: Condens. Matter* **19**, 323101 (2007).
- [3] Hsiao, L. C., R. S. Newman, S. C. Glotzer, and M. J. Solomon, “Role of isostaticity and load-bearing microstructure in the elasticity of yielded colloidal gels,” *PNAS* **109**(40), 16029-16034 (2012).
- [4] Park, J. D., and K. H. Ahn, “Structural evolution of colloidal gels at intermediate volume fraction under startup of shear flow,” *Soft Matter* **9**, 11650-11662 (2013).
- [5] Park, J. D., S. J. Lee, and K. H. Ahn, “Structural change and dynamics of colloidal gels under oscillatory shear flow,” *Soft Matter* **11**, 9262-9272 (2015).
- [6] Koumakis, N., and G. Petekidis, “Two step yielding in attractive colloids: transition from gels to attractive glasses,” *Soft Matter* **7**, 2456-2470 (2011).
- [7] Bonn, D., J. Paredes, M. M. Denn, L. Berthier, T. Divoux, and S. Manneville, “Yield stress materials in soft condensed matter,” arXiv:1502.05281v1 (2015).
- [8] Kim, J. M., A. R. Eberle, A. K. Gurnon, L. Pocar, and N. J. Wagner, “The microstructure and rheology of a model, thixotropic nanoparticle gel under steady shear and large amplitude oscillatory shear (LAOS),” *J. Rheol.* **58**(5), 1301-1328 (2014).
- [9] Gopalakrishnan, V., and C. F. Zukoski, “Delayed flow in thermo-reversible colloidal gels,” *J. Rheol.* **51**(4), 623–644 (2007).
- [10] Woutersen, A., R. P. May, and C. G. Dekruif, “The shear-distorted microstructure of adhesive hard-sphere dispersions: A small-angle neutron-scattering study,” *J. Rheol.* **37**(1), 71-88 (1993).
- [11] Varadan, P., and M. J. Solomon, “Shear-induced microstructural evolution of a thermoreversible

- colloidal gel,” *Langmuir* **17**(10), 2918–2929 (2001).
- [12] Hoekstra, H., J. Mewis, T. Narayanan, and J. Vermant, “Multi length scale analysis of the microstructure in sticky sphere dispersions during shear flow,” *Langmuir* **21**(24), 11017-11025 (2005).
- [13] Eberle, A. P. R., N. Martys, L. Porcar, S. Kline, J. M. Kim, P. D. Butler, N. Valadez, R. Castaneda-Priego, and N. J. Wagner, “Shear viscosity and structural scaling in model adhesive hard-sphere gels,” *Phys. Rev. E* **89**(5), 050302(R) (2014).
- [14] Hoekstra, H., J. Vermant, and J. Mewis, “Flow-induced anisotropy and reversible aggregation in two-dimensional suspensions,” *Langmuir* **19**(22), 9134-9141 (2003).
- [15] Masschaele, K., J. Fransaer, and J. Vermant, “Flow-induced structure in colloidal gels: Direct visualization of model 2D suspensions,” *Soft Matter* **7**, 7717-7726 (2011).
- [16] Koumakis, N., E. Moghimi, R. Besseling, W. C. K. Poon, J. F. Brady, and G. Petekidis, “Tuning colloidal gels by shear,” *Soft Matter* **11**, 4640–4648 (2015).
- [17] Foss, D. R., and J. F. Brady, “Structure, diffusion, and rheology of Brownian suspensions by Stokesian Dynamics simulation,” *J. Fluid Mech.* **407**,167-200 (2000).
- [18] Koumakis, N., M. Laurati, A. R. Jacob, K. J. Mutch, A. Abdellali, A. B. Schofield, S. U. Egelhaaf, J. F. Brady, and G. Petekidis, “Start-up shear of concentrated colloidal hard spheres: Stresses, dynamics, and structure,” *J. Rheol.* **60**, 603-623 (2016).
- [19] Lin, N. Y. C., M. Bierbaum, P. Schall, J. P. Sethna, and I. Cohen, “Measuring nonlinear stresses generated by defects in 3D colloidal crystals,” *Nature Mater.* **15**, 1172-1176 (2016).
- [20] Mohraz, A., and M. J. Solomon, “Orientation and rupture of fractal colloidal gels during startup of steady shear flow,” *J. Rheol.* **49**(3), 657-681 (2005).
- [21] Seth, J. R., L. Mohan, C. Locatelli-Champagne, M. Cloitre, and R. T. Bonnecaze, “A micro mechanical model to predict the flow of soft particle glasses,” *Nature Mater.* **10**, 838-843 (2011).
- [22] Mohan, L., C. Pellet, M. Cloitre, and R. T. Bonnecaze, “Local mobility and microstructure in periodically sheared soft particle glasses and their connection to macroscopic rheology,” *J. Rheol.* **57**(3), 1023-1046 (2013).

- [23] Koumakis, N. M. Laurati, S. U. Egelhaaf, J. F. Brady, and G. Petekidis, “Yielding of Hard-Sphere Glasses during Start-up shear,” *Phys.Rev. Lett.* **108**(9), 098303 (2012).
- [24] Gurnon, A. K., and N. J. Wagner, “Microstructure and rheology relationship for shear thickening colloidal dispersions,” *J. Fluid. Mech.* **769**, 242-276 (2015).
- [25] Gurnon, A. K., C. R. López-Barron, A. P. R. Eberle, L. Porcar, and N. J. Wagner, “Spatiotemporal stress and structure evolution in dynamically sheared polymer-like micellar solutions,” *Soft Matter* **10**, 2889–2898 (2014a).
- [26] Helgeson, M. E., P. A. Vasquez, E. W. Kaler, and N. J. Wagner, “Rheology and spatially resolved structure of cetyltrimethylammonium bromide wormlike micelles through the shear banding transition,” *J. Rheol.* **53**(3), 727-756 (2009).
- [27] Pignon, F., A. Magnin, and J. M. Piau, “Butterfly light scattering pattern and rheology of a sheared thixotropic clay gel,” *Phys. Rev. Lett.* **79**(23), 4689-4692 (1997).
- [28] Pignon, F., A. Magnin, and J. M. Piau, “Thixotropic behavior of clay dispersions: Combinations of scattering and rheometric techniques,” *J. Rheol.* **42**(6), 1349-1373 (1998).
- [29] Cheng, X., X. Xu, S. A. Rice, A. R. Dinner, and I. Cohen, “Assembly of vorticity-aligned hard-sphere colloidal strings in a simple shear flow,” *PNAS* **109**(17), 63-67 (2012).
- [30] Pantina, J. P., and E. M. Furst, “Elasticity and critical bending moment of model colloidal aggregates,” *Phys.Rev. Lett.* **94**(13), 138301 (2005).
- [31] Whittle, M., and E. Dickinson, “Large deformation rheological behavior of a model particle gel,” *J. Chem. Soc., Faraday Trans.* **94**(16), 2453-2462 (1998).
- [32] Whittle, M., and E. Dickinson, “Brownian dynamics simulation of gelation in soft sphere systems with irreversible bond formation,” *Molecular. Phys.* **90**(5), 739-757 (1997).
- [33] Allen, M., and D. Tildesley, *Computer Simulation of liquids* (Oxford University Press, Oxford, 1987).
- [34] Tanaka, H., and T. Araki, “Simulation Method of Colloidal Suspensions with Hydrodynamic Interactions: Fluid Particle Dynamics,” *Phys. Rev. Lett.* **85**(6), 1338-1341 (2000).

- [35] Varga, Z., and J. Swan, “Hydrodynamic interactions enhance gelation in dispersions of colloids with short-ranged attraction and long-range repulsion,” *Soft Matter* **12**, 7670-7681 (2016).
- [36] Hess, S., and H. J. M. Hanley, “Pressure tensor and viscosity coefficients of a soft sphere liquid under shear,” *International Journal of Thermophysics* **4**(2), 97-114 (1983).
- [37] Wagner, N. J., and B. J. Ackerson, “Analysis of nonequilibrium structures of shearing colloidal suspensions,” *J. Chem. Phys.* **97**(2), 1473–1483 (1992).
- [38] Hanley, H. J. M., and J. C. Rainwater, “Shear induced angular dependence of the liquid pair correlation function,” *Phys. Rev. A* **36**(4), 1795-1805 (1987).
- [39] Rainwater, J. C., H. J. M. Hanley, and S. Hess, “The static structure factor of a soft sphere liquid under shear,” *Physics Letters A* **126**(8), 450-454 (1988).
- [40] López-Barrón, C. R., A. K. Gurnon, A. P. R. Eberle, L. Porcar, and N. J. Wagner, “Microstructural evolution of a model, shear banding micellar solution during shear startup and cessation,” *Phys. Rev. E* **89**(4), 042301 (2014).
- [41] Walker, L. M., and N. J. Wagner, “SANS analysis of the molecular order in poly/Deuterated Dimethylformamide under shear and during relaxation,” *Macromolecules* **29**(6), 2298-2301 (1996).
- [42] Zia, R. N., B. J. Landrum, and W. B. Russel, “A micro-mechanical study of coarsening and rheology of colloidal gels: Cage building, cage hopping, and Smoluchowski’s ratchet,” *J. Rheol.* **58**(5), 1121-1157 (2014).
- [43] Fielding, S. M., P. Solich, and M. E. Cates, “Aging and rheology in soft materials,” *J. Rheol.* **44**(2), 323- 369 (2000).
- [44] Solich, P., F. Lequeux, P. Hebraud, and M. E. Cates, “Rheology of soft glassy materials,” *Phys. Rev. Lett.* **78**(10), 2020-2023 (1997).
- [45] Solich, P., “Rheological constitutive equation for a model of soft glassy materials,” *Phys. Rev. E* **58**(1), 738-759 (1998).
- [46] Viasnoff, V., and F. Lequeux, “Rejuvenation and overaging in a colloidal glass under shear,”

- Phys. Rev. Lett. **89**(6), 065701 (2002).
- [47] Viasnoff, V., S. Jurine, and F. Lequeux, “How are colloidal suspensions that age rejuvenated by strain application?,” *Faraday Discuss.* **123**, 253–266 (2003).
- [48] Yin, G., and M. J. Solomon, “Soft glassy rheology model applied to stress relaxation of a thermoreversible colloidal gel,” *J. Rheol.* **52**(3), 785-800 (2008).
- [49] Morris, J. F., and B. Katyal, “Microstructure from simulated Brownian suspension flows at large shear rate,” *Phys. Fluid* **14**(6), 1920-1937 (2002).
- [50] Xu, B., and J. F. Gilchrist, “Microstructure of sheared monosized colloidal suspensions resulting from hydrodynamic and electrostatic interactions,” *J. Chem. Phys.* **140**(20), 204903 (2014).
- [51] Dhont, J. K. G., *An introduction to dynamics of colloids* (Elsevier, Amsterdam, 2003)
- [52] Gurnon, A. K., M. J. Wasbrough, C. R. Lopez-Barron, L. Porcar, and N. J. Wagner, “Spatially resolved concentration and segmental flow alignment in a shear-banding solution of polymer-like micelles,” *ACS Macroletters* **3**(3), 276-280 (2014).
- [53] de Souza Mendes, P. R., “Modeling the thixotropic behavior of structured fluids,” *J. Non-Newtonian Fluid Mech.* **164**, 66–75 (2009).
- [54] Dullaert, K., and J. Mewis, “A structural kinetics model for thixotropy,” *J. Non-Newtonian Fluid Mech.* **139**, 21-30 (2006).
- [55] Mewis, Jan., and N. J. Wagner, *Colloidal suspension rheology* (Cambridge University Press, Cambridge, 2012).
- [56] Goodeve, C. F., “A General Theory of Thixotropy and Viscosity,” *Trans. Faraday Society* **35**, 342-358 (1939).